UMUTEME, O.M., ISLAM, S.Z., HOSSAIN, M. and KARNIK, A. 2022. An improved computational fluid dynamics (CFD) model for predicting hydrate deposition rate and wall shear stress in offshore gas-dominated pipeline. *Journal of natural gas science and engineering* [online], 107, article 104800. Available from: https://doi.org/10.1016/j.jngse.2022.104800

An improved computational fluid dynamics (CFD) model for predicting hydrate deposition rate and wall shear stress in offshore gas-dominated pipeline.

UMUTEME, O.M., ISLAM, S.Z., HOSSAIN, M. and KARNIK, A.

2022

Journal of Natural Gas Science and Engineering 107 (2022) 104800

Contents lists available at ScienceDirect

Journal of Natural Gas Science and Engineering

journal homepage: www.elsevier.com/locate/jngse

An improved computational fluid dynamics (CFD) model for predicting hydrate deposition rate and wall shear stress in offshore gas-dominated pipeline

Oghenethoja Monday Umuteme, Sheikh Zahidul Islam *, Mamdud Hossain, Aditya Karnik

School of Engineering, Robert Gordon University, Aberdeen, AB10 7GJ, UK

ARTICLE INFO

Keywords:
Hydrate deposition rates
Computational fluid dynamics
Hydrate plugging and pipe blockage
Gas consumption
Gas solubility in water
Wall shear stress

ABSTRACT

Gas hydrates in pipelines is still a flow assurance problem in the oil and gas industry and requires a proactive hydrate plugging risk predicting model. As an active area of research, this work has developed a 3D 10 m length by 0.0204 m diameter horizontal pipe CFD model based on the eulerian-eulerian multiphase modelling framework to predict hydrate deposition rate in gas-dominated pipeline. The proposed model simulates the conditions for hydrate formation with user defined functions (UDFs) for both energy and mass sources implemented in ANSYS Fluent, a commercial CFD software. The empirical hydrate deposition rates predicted by this model at varying subcooling temperatures and gas velocities are consistent with experimental results within ±10% uncertainty bound. At lower gas velocity of 4.7 m/s, the model overpredicted the hydrate deposition rates of the experimental results in Aman et al. (2016) by 9–25.7%, whereas the analytical model of Di Lorenzo et al. (2018) underpredicted the same experimental results by a range of 27–33%. Consequently, the CFD model can enhance proactive hydrate plugging risk predictions earlier than the analytical model, especially at low gas productivity. Similarly, at a velocity of 8.8 m/s and subcooling temperatures of 2.5 K, 7.1 K and 8.0 K, the CFD model underpredicted the hydrate deposition rates of the regressed experimental results in Di Lorenzo et al. (2014a) by 14%, 6% and 4% respectively, and overpredicted the results by 1% at a subcooling temperature of 4.3 K. From the CFD model results, we also suggest that hydrate sloughing shear stress is relatively constant, and the wall shedding shear stress by hydrate vary during deposition. Finally, the CFD model also predicted the phase change during hydrate formation, agglomeration, and deposition.

1. Introduction-

The need for a specific gas-hydrate predicting model for gas-dominated systems has been stressed in the literature (Charlton et al., 2018a). Natural gas is still preferred as a cleaner source of energy when compared to coal and crude oil for its lower carbon level. Whereas hydrogen gas is cleaner, yet transportability concerns for large-scale industry application continue to favour the use of natural gas (Melaina et al., 2013; Meng et al., 2017; Umuteme, 2020). In 2020, global demand for natural gas was estimated as 4.4 trillion cubic meters (BP, 2020). As the world move into a fully digital economy, the dependence on natural gas will continue to increase. While waiting for other competitive sources of energy that can meet global energy demand in the coming years, it is important to enhance flow assurance in natural gas pipelines through proactive intervention measures that can manage the formation and deposition of hydrates. Gas hydrates are still operational pipeline plugging risk in the transportation of natural gas. For offshore gas pipelines buried or lying on the seabed, subcooling temperatures around the pipeline can lead to gas-pipewall thermal gradient that can increase the formation and deposition of hydrates. This occurrence can hinder gas availability to costumers. Also, pipeline plugging and reduction of hydraulic diameter during hydrates deposition can lead to pipeline failure through over-pressurisation (Jassim et al., 2010; Sloan et al., 2011a). Thus, hydrate deposition in gas-dominated pipelines is one of the prevailing safety and economic concerns in the oil and gas industry (Koh and Creek, 2011). This has led to increase in research activity in this area to improve the knowledge of how hydrate formation and deposition can affect flow assurance in gas pipelines. Currently, three approaches are implemented in the industry to management hydrates, including hydrate prediction, prevention and problem solving (Kinnari et al., 2015). Firstly, hydrate prediction is

---

* Corresponding author.
E-mail address: s.z.islam1@rgu.ac.uk (S. Zahidul Islam).

https://doi.org/10.1016/j.jngse.2022.104800
Received 9 June 2021; Received in revised form 14 September 2022; Accepted 19 September 2022

Nomenclature

A	Pipe cross-sectional area (m^2)
A_i	Interfacial area (m^2)
L	Length of the pipe covered by dispersed liquid and liquid film at the pipe wall (m)
C_μ	Turbulent viscosity constant (dimensionless)
$C_{1\varepsilon}$ $C_{2\varepsilon}$ and $C_{3\varepsilon}$	Constants (dimensionless)
D	Diameter of the pipe section prone to hydrate formation (m)
$D_{t,pq}$	Binary diffusivity ($D_{t,pq} = \frac{1}{3}K_{pq}\tau_{t,pq}$) (Pa)
$G_{k,q}$	Turbulent kinetic energy production term per phase (dimensionless)
h_q	The q^{th}phase specific enthalpy (J/kg)
h_{pq}	Interphase enthalpy (J/kg)
K_{pq}	Covariance of the phase velocities (dimensionless)
k_1 and k_2	Constants (dimensionless)
K_{ex_factor}	Extrapolation factor
k	Turbulent kinetic energy rate (m^2s^{-3})
k	Turbulent kinetic energy (J/kg)
$\dot{m}_{CH_4}$	Methane gas consumption rate ($\frac{dm_g}{dt}$) (Kg/s)
$\dot{m}_{pq}$	Rate of mass transfer from the $p^{th}$to the q^{th} phase (Kg/s)
$\dot{m}_{qp}$	Rate of mass transfer from the q^{th} to the p^{th} phase (Kg/s)
P_{eq}	Hydrate formation equilibrium pressure (KPa)
v_g	Velocity of the primary continuous gas phase (m/s)
$\overrightarrow{\vartheta}_q$	Velocity vector of the phase in the control volume (m/s)
$\overrightarrow{v}_{dr}$	Drift velocity vector between the gas and liquid phase (m/s)
$\overrightarrow{v}_{pq}$	Relative velocity vector between both phases (m/s)
Q_H	Hydrate formation, agglomeration and deposition rate (L/min)
Q_{pq}	Intensity of the heat exchange between the phases (W)
$\overrightarrow{q}_q$	Heat flux vector (W/m^2)
S_q	Source/sink term: gas consumption rate or source energy rate (Kg/s-m^3 or J/s-m^3)
T_{eq}	Hydrate formation equilibrium temperature (K)
T_{sys}	System temperature (K)

Greek Symbol

α_q	Phase fraction (dimensionless)
$\frac{\partial p_q}{\partial t}$	Transient pressure of the qth phase(Pa/s)
ε	Turbulent dissipation rate (m^2s^{-3})
ρ_{H_hwc}	Density of hydrate in the hydrate-water composite (kg/m^3)
ρ_q	Density of the phase (kg/m^3)
ρ_q	Density of the qth phase (kg/m^3)
$\widetilde{\rho}$	Averaged density (kg/m^3)
μ_{tq}	Turbulent viscosity of the qth phase (Nm^{-2}.s, Pa.s)
ΔT_{sub}	Sub-cooling temperature (K)
$\varphi_{\mathscr{U}}$ & φ_p	velocity & pressure under-relaxation factors respectively
ΔH_{Hyd}	Enthalpy of hydrate generation (J/kg)
∇_{α_p} and ∇_{α_q}	Variations in concentration of the gas and liquid phase respectively
Π_{kq} and $\Pi_{\varepsilon q}$	Source terms for the turbulence interactions of the entrained water phase on the primary gas phase (Π_{kq}: turbulent and $\Pi_{\varepsilon q}$: dissipation)
σ_{kq} and $\sigma_{\varepsilon q}$	Ratio of the temperature-dependent kinematic eddy viscosity of the continuous gas phase to the dispersed liquid phase. σ_{kq} is turbulent kinetic energy (TKE) and $\sigma_{\varepsilon q}$ turbulent dissipation rate (TDR) Prandtl numbers (dimensionless)
$\tau_{t,pq}$	eddy particle interaction time
τ_c^t	turbulent stress of the carrier (gas) phase

related to how hydrates are formed and the safety concerns, such as pressure rise and pipeline rupture (Di Lorenzo et al., 2014b; Kinnari et al., 2015). Hydrate prediction is important in estimating the capacity utilization and optimization of hydrate-prone gas pipelines (Umuteme and Umeh, 2019). Secondly, hydrate prevention in gas pipelines is possible by modifying the flow parameters and conditions, such as temperature, pressure and gas flowrate (Carroll, 2014; Lederhos et al., 1996; Li et al., 2013; Lim et al., 2020). Thirdly, problem solving approach to hydrate management in the oil and gas industry is cost intensive and not usually recommended for effective hydrate control (Jassim et al., 2010; Kinnari et al., 2015).

Hydrate formation kinetics and growth models provides the foundation knowledge for understanding the flow behaviour of hydrates in pipelines, and are discussed extensively in the literature (Carroll, 2014; Sloan et al., 2011b; Yin et al., 2018). Recent advances exist in experimental research (Aman et al., 2016; Di Lorenzo et al., 2014a, 2014b; Ding et al., 2017; Li et al., 2013; Liu et al., 2020; Odutola et al., 2017; Zhang et al., 2017) and analytical models (Di Lorenzo et al., 2018; Liu et al., 2019; Wang et al., 2017, 2018) on hydrate formation and deposition rates in gas pipelines. The experimental study of hydrates in gas pipelines is usually a difficult task (Lim et al., 2020) and expensive because, changing the experimental pipe geometry, such as length and diameter, requires new or modified experimental set up. Thus, increasing the difficulty in extrapolating experimental results for large scale field application. Consequently, analytical models have gained research attention lately leading to the following significant findings: (i) sloughing and shedding of the deposits of hydrates is responsible for the fluctuation in the shear strength of hydrates (Liu et al., 2019) and transient pressure drop in the pipe (Di Lorenzo et al., 2018; Liu et al., 2019); (ii) hydrate deposition and growth generate the following multiphase flows, including: 3-phase gas-water-hydrates; 2-phase gas-hydrate; and 2-phase water-saturated gas. The authors suggested that the plugging risk of hydrates is more likely in the 3-phase gas-water-hydrates flow (Wang et al., 2018); (iii) the thickness of hydrates along the pipe wall follows a non-uniform pattern, and about fifty-percent (50%) of the hydrates deposited are formed at the dispersed water in the gas phase (Wang et al., 2017); and (iv) increasing the gas velocity increases the depositional distance from the point of hydrates generation along the pipeline (Jassim et al., 2010). However, only the analytical models developed by Di Lorenzo et al. (2018) and Wang et al. (2018) focused on hydrates deposition rates in gas dominated pipeline at different subcooling temperatures, which is relevant for estimating the plugging flowtime of hydrates and the resulting transient pressure drop. Both models predicted deposition rates of hydrates comparatively with experimental results. However, only the model by Di Lorenzo et al. (2018) considered hydrates deposition rates at low gas velocity of 4.7 m/s, yet the tweaking of the model through multiplier parameters to predict experimental results is a concern for scalability and extension for industrial size pipelines. Consequently, the model underpredicted all the experimental results of Aman et al. (2016) at the gas velocity of 4.7 m/s and subcooling temperature range of 4.5–7.5 K. After predicting the first experimental result of 0.055 L/min as 0.04 L/min at the subcooling temperature of 4.5 K, the model predicted the hydrates deposition rate of 0.07 L/min against the experimental value of 0.105 L/min at 7.5 K subcooling temperature under the same gas velocity of 4.7 m/s. This imply that the model is unreliable at higher subcooling temperature and low gas productivity, which is a concern raised in the literature (Li et al., 2021). Thus, the extension of this model for industrial application can underpredict hydrate plugging risk under similar flow condition, with attendant consequences that were discussed earlier.

Therefore, the increasing availability of various CFD software necessitated the need for a validated CFD model that can accurately predict hydrate deposition rate in gas pipelines. Progress in CFD modelling of hydrates in gas pipelines has focused on the deposition and transportability of hydrates, and not on hydrates deposition rates. A CFD model capable of accurately predicting hydrates deposition rates and wall shear stress during hydrates deposition can provide additional insights into hydrates plugging risks in gas pipelines. However, progress in related CFD models is relatively lacking. Recent advancement in CFD modelling are discussed as follows. Balakin et al. (2016) developed a CFD model for the agglomeration and deposition of hydrates using the population balance method (PBM) in oil-dominated pipelines. Though the results were validated with experimental data, the model was developed for oil-dominated pipelines and did not predict hydrates deposition rates by direct simulation of hydrates temperature and pressure conditions. Other oil-dominated hydrate deposition CFD models reported in the literature (e.g., Lo, 2011; Neto et al., 2015; Song et al., 2018a), are not suitable for predicting hydrates deposition in gas pipelines because of the difference in multiphase flow in oil-dominated pipeline (oil-gas-water) and gas-dominated pipeline (gas-water). For gas-dominated pipelines, Jassim et al. (2010) developed a CFD model that determines the distribution of fluid properties in the flow domain during the formation and deposition of hydrates to calculate the particle size distribution and depositional distance of hydrates along the pipeline. The hydrates deposition CFD model by Neto et al. (2016) provided insight into the nature of hydrates slurry settling at the bottom in a gas pipeline, but the model was not validated. Also, the model did not simulate the annular effect of hydrate growth on the pipe wall reported from experimental observations (Aman et al., 2016; Di Lorenzo et al., 2014a). Other CFD models for hydrates studies in gas pipelines neglected the formation of hydrates but focused on the agglomeration, deposition, rheology, and transportability of hydrates by injecting hydrates into the flow domain as a discrete phase (e.g., Berrouk et al., 2020; Jujuly et al., 2017; Li et al., 2019; Song et al., 2018b; Sule et al., 2015).

Thus, the CFD model developed in this paper is timely for the following reasons. First, the predictions of the only analytical model that predicted hydrates deposition rates at lower velocity of 4.7 m/s underpredicted experimental result at higher subcooling temperatures of 7.5 K by 33%, thus exposing the pipeline under this condition to underpredicted hydrate plugging risk. Second, existing CFD models injected hydrates into the flow domain as a discreet phase. While this approach predicts hydrate velocity distribution, deposition, agglomeration, and transportability of hydrates, it is not adequate for transient simulation prediction of hydrate plugging risk based on the temperature and pressure conditions in the pipeline. Third, this CFD model simulation aim to clarify the disagreement in the literature on whether the wall shear stress varies (Liu et al., 2019) or is constant (Di Lorenzo et al., 2018) during the deposition of hydrates along the pipeline. This is important for future studies that aim to model the impact of gas and water-induced shear stress on the plugging risk of hydrates in gas pipelines.

Although there are currently no validated CFD models to predict the depositional rates of hydrates, research evidence indicates that CFD transport and energy equations, and other physical models that defines the intensive and extensive properties of the fluid medium can be implemented in CFD modelling of hydrate deposition in gas pipelines. The CFD model developed in this study for predicting hydrate deposition rates in a gas pipeline is based on the conditions for hydrate formation in the literature (Carroll, 2014): (a) adequate combination of low temperature and high pressure based on the composition of the natural gas; (b) availability of gas hydrate formers (e.g., methane, ethane, and carbon-dioxide); and (c) presence of water in sufficient amount. The formation of hydrates is equally enhanced by flow and physical parameters such as turbulence and agitation, hydrate nucleation sites (elbows, Tees, and valves) and water-gas interface (Carroll, 2014). Furthermore, the gas consumption rate during hydrate formation is dependent on the increasing solubility of methane gas in water at higher pressure and lower temperatures below the equilibrium point on the hydrate formation loci (Lekvam and Bishnoi, 1997).

Additionally, experimental results suggests that the growth of hydrates is dependent on the temperature driving force and gas–water interfacial area (Aman et al., 2016; Di Lorenzo et al., 2014a, 2014b; Ding et al., 2017; Turner et al., 2005; Zhang et al., 2017).The thermal gradient between the temperature of the wet gas and pipe wall influences the induction time during the initiation and growth of hydrates (Lim et al., 2020). Also, the pipeline environment creates the sub-cooling temperature, which results in the thermal transfer by convection during the turbulent interaction between the water phase and the continuous gas phase. Thus, the increase in the solubility of natural gas in water is initiated by the thermal cooling at the pipe wall due to increasing sub-cooling temperatures from the environment. In their flowloop experiment, Odutola et al. (2017) reported that at the commencement of hydrate formation, the temperature decreased until it was stable during the agglomeration and deposition of hydrates. This position is also corroborated in an earlier experiment by Li et al. (2013) and recently by Liu et al. (2020). Furthermore, Ding et al. (2017) reports a range of 771–830 kg/m^3 as the density of hydrates during deposition. Earlier, Li et al. (2013) reported a range of 805–825 kg/m^3. From both studies, an average value of 807.75 kg/m^3 is obtained as the density of hydrates. However, this study adopted a similar hydrate density of 807.77 kg/m^3 used in the CFD-PBM simulation in Balakin et al. (2016). Furthermore, visual inspection during experimental runs indicates an annular-dispersed flow pattern during hydrate formation and deposition (Aman et al., 2016; Di Lorenzo et al., 2014a, 2014b; Ding et al., 2017).

Therefore, this research is on the formulation of a CFD model for predicting hydrate deposition rates and the resulting wall shear stress in the horizontal section of an offshore hydrate-forming gas pipeline by simulating the thermo-mechanistic multiphase (methane and water) flow conditions for the formation of hydrates. Through the implementation of user defined function (UDF) codes for the mass and energy sources in a commercial CFD software package (ANSYS Fluent), metered gas injection into the computational domain was controlled to mimic the gas consumption rate during hydrate formation. This effect was enhanced by the increasing density of gas towards the pipe wall by momentum and thermal diffusivity, as the solubility of methane in water increases at lower subcooling temperatures and high pressure. Using a mathematical relation, the resulting simulated average gas mass flowrate was converted to average deposition rates of hydrates in L/min. The final results are validated with experimental and analytical results available in the literature (Aman et al., 2016; Di Lorenzo et al., 2014a, 2018). Sensitivity analyses was carried out to improve the understanding of the effect of velocity and temperature on the depositional rates of hydrates, the resulting transient pressure drop and wall shear stress, and to establish the predictability of the CFD model based on parameter variability. Thus, the focus of this research paper is to accurately predict hydrate deposition rate and the resulting pipe wall shear stress, as both are important flow assurance phenomenon for gas pipelines in the oil and gas industry. The rest of the paper is structured as follows – the methodology is discussed in section 2 and followed by the discussion of the results and validations in section 3. Finally, the conclusion and recommended gap for future studies is presented in section 4.

2. Methodology-

2.1. CFD model development

The main assumptions in the development of this model are as follows. (i) One simplifying assumption of the analytical model by Di Lorenzo et al. (2018) is that the compositional changes in the gas phase during the formation of hydrates was not considered. This can affect the prediction of hydrate deposition under different conditions of gas velocity and subcooling temperature. Instead, the authors adopted an empirical hydrate deposition tuning parameter which was not sensitive to changes in subcooling temperature at low gas velocity. To overcome this challenge, this study introduced mass and energy UDF codes into the software to ensure that the gas flowrate in the fluid domain is related to the gas velocity and subcooling temperature; (ii) The accuracy of the model is dependent on the resulting increase in pressure drop during the agglomeration of hydrates. Since the model adopted a pressure-velocity coupling CFD simulation technique, the stability of the model at higher gas velocity was achieved by choosing a mesh size with the least pressure drop; and (iii) The interpretation of the contour profiles generated by the CFD model was based on an earlier assumption in the literature (Di Lorenzo et al., 2018), that hydrate deposits grows radially inwards in the pipeline.

Two methods for estimating hydrate formation rates include the mass transport limited model (Skovborg and Rasmussen, 1994) and kinetics models (e.g., Turner et al., 2005). However, the results of the kinetics model compared more favourably with the results of the experiments in the literature (Aman et al., 2016; Di Lorenzo et al., 2014a; Wang et al., 2018), which were used for the validation of the CFD Model. Empirical observations suggests that a relatively stable temperature and increasing transient pressure is expected during the agglomeration of hydrates as a result of turbulent hydraulic loading of hydrates in the continuous gas phase and the deposition of hydrates on the wall (Li et al., 2013; Liu et al., 2020; Odutola et al., 2017; Turner and Talley, 2008; Zerpa et al., 2013). In this study, the UDF mass and energy sources are programmed to control gas flowrate in the fluid domain under hydrates formation, agglomeration, and deposition conditions. Three parameters were observed during the simulation, including the gas mass flowrate in the fluid domain, the rise in system absolute pressure drop, and a relatively stable gas temperature.

This study is based on the eulerian-eulerian multiphase framework with boundary conditions and physical flow parameters implemented mainly to enhance interfacial gas-water interaction Previous CFD simulations on gas hydrates adopted the eulerian-eulerian approach as the most appropriate for interfacial gas-water interaction (e.g., Neto et al., 2016; Berrouk et al., 2020). The boundary conditions implemented in this study are from the experiments by Di Lorenzo et al. (2014b, 2014a) and Aman et al. (2016), as provided in Table 4: water volume fraction of 0.06, gas velocities of 4.7 m/s and 8.8 m/s, operating pressure of 8.8 MPa and gas temperature of 292 K. The results from the experiments where recently used in validating the results of the analytical models by Wang et al. (2017), Di Lorenzo et al. (2018) and Liu et al. (2019). The overall aim of this study is to extend the CFD model for the design, operation, and maintenance planning of hydrate-forming gas pipelines. The stages adopted in the development of this model are presented in Fig. 1, below.

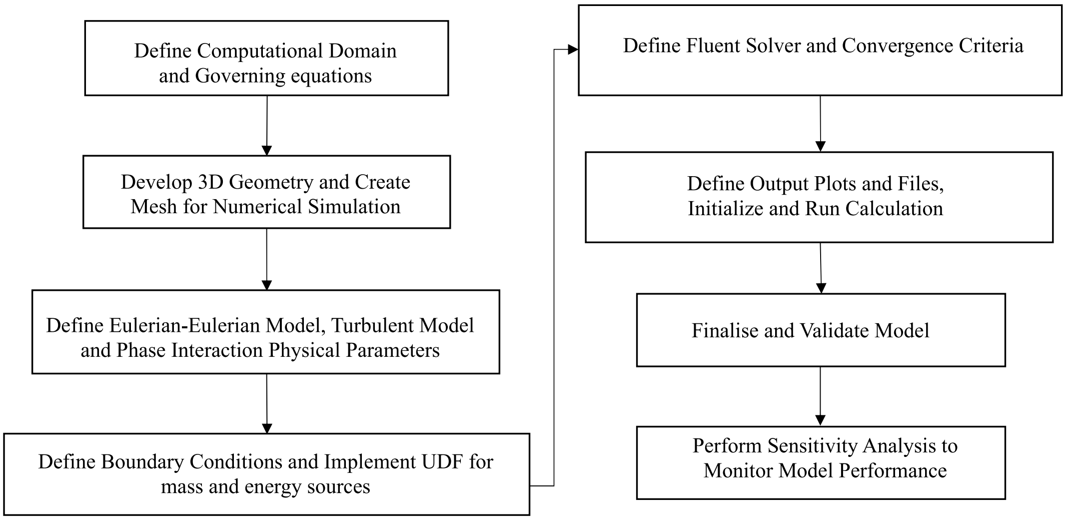

Fig. 1. Cfd model development stages.

2.2. *Computational domain*

A schematic of a 2D slice and 3D mesh cells of the CFD computational domain are represented below in Fig. 2 and Fig. 3 respectively. The domain is 10 m length (L) pipe, with diameter (D) of 0.0204 m and pipewall thickness of 0.0012 m. For flow stabilization in many practical engineering turbulent flow problems, the entrance length (L_e) is estimated for a pipe of diameter (D) as $20\text{D} < L_e < 30\text{D}$ (Munson et al., 2013). Using 30D as maximum, the L_e is computed as 0.612 m, implying that a 10 m length of a 0.0204 m diameter pipe is adequate for the CFD simulation. The multiphase fluid is water and natural gas. Inlet variable is defined as velocity, while outlet monitored variable is pressure.

2.3. *Governing equations*

Hydrates are formed when the solubility of natural gas in water increases under hydrate-forming temperature and pressure condition, as discussed earlier. Hence, based on eulerian-eulerian interfacial interaction between gas and water, a 2-phase flow is the initial multiphase fluid at the inlet of the model. The resulting governing equations are discussed in this section.

Continuity Equation:

The mass continuity equation (Fluent Theory, 2017), is represented below:

$$\frac{\partial}{\partial t}\left(\alpha_q\rho_q\right)+\nabla.\left(\alpha_q\rho_q\vec{\vartheta}_q\right)=\sum_{p=1}^{n}\left(\dot{m}_{pq}+\dot{m}_{qp}\right)+S_q \tag{1}$$

where α_q is the phase fraction; $\vec{\vartheta}_q$ is the velocity (m/s) of the phase in the control volume; ρ_q is the density (kg/m^3) of the respective phase; S_q is the source/sink term, which is "zero" for implicit multiphase flow modelling; $\dot{m}_{pq}$ is the mass transfer rate from the p^{th} to the q^{th} phase and $\dot{m}_{qp}$ is mass transfer (kg/s) from the q^{th} phase to the p^{th} phase. $\sum_{p=1}^{n}(\dot{m}_{pq}+\dot{m}_{qp})$ is equal to "zero," because this study assumes no interphase mass transfer (Balakin et al., 2016), but the gas consumption rate is solely dependent on the gas mass source, S_q.

The rate of gas consumption (kg/s) is also the hydrate formation rate as reported by Turner et al. (2005) in Eq. (2). The authors developed this

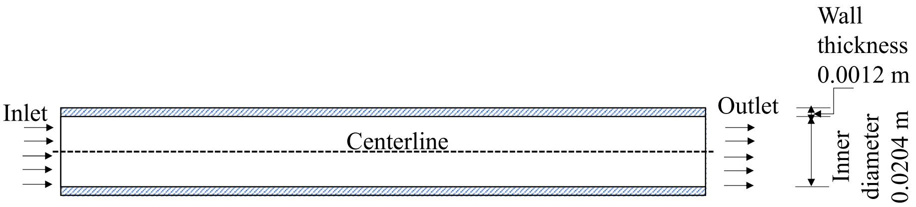

Fig. 2. 2D representation of the computational domain (dimensions are not to scale).

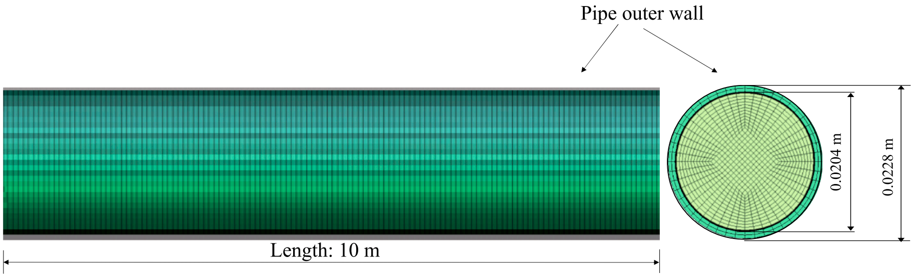

Fig. 3. 900,000 cells 3D mesh computational domain (dimensions are not to scale).

relation based on the assumption that the hydrates were formed at the condensed water-saturated gas phase only. In this study, the gas consumption rate is positively and proportionally related to the CFD computed gas mass flow rate.

$$\dot{m}_{CH_4} = \frac{dm_g}{dt} = -k_1\, exp\left(\frac{k_2}{T_{sys}}\right).\, A_i \Delta T_{sub} \tag{2}$$

where $\dot{m}_{CH_4}$ is the gas consumption rate ($\frac{dm_g}{dt}$; kg/s); k_1 and k_2 are constants; and A_i is the interfacial area (m^2). For methane hydrates, the regressed values based on the experimental measurements of Vysniauskas and Bishnoi (1983) are: $k_1 = 7.3548 \times 10^{17}$ and $k_2 = -13{,}600$ K (Zerpa et al., 2013, p.301). The thermal driving force for hydrate formation as proposed in Turner et al. (2005) is the sub-cooling temperature "ΔT_{sub}"in Kelvin, expressed as:

$$\Delta T_{sub} = T_{eq} - T_{sys} \tag{3}$$

where T_{eq} and T_{sys} are hydrate formation equilibrium and system temperatures respectively. The hydrate deposition rates in m^3/s, is the quotient of the simulated gas mass flow rate, $\dot{m}_{CH_4}$ (kg/s), divided by the hydrate density of 807.77 kg/m^3 (Balakin et al., 2016).

$$\dot{m}_{CH_4}\left(\frac{\text{m}^3}{\text{s}}\right) = \frac{\dot{m}_{CH_4}\left(\frac{\text{kg}}{\text{s}}\right)}{807.77\left(\frac{kg}{m^3}\right)} \tag{4}$$

The interfacial area (A_i) was estimated from the sum of the entrained droplets and liquid film at the wall. This is because hydrates form from both the annular wetting film on the pipe-wall and the entrained droplets (Wang et al., 2017). From the results obtained for the interfacial area in Aman et al. (2016), the interfacial area for this study was approximated as:

$$A_i = (2.941 v_g - 8.824) LD \tag{5}$$

where L is the Length (m) of the pipe covered by dispersed liquid and liquid film at the pipe wall; D is the Diameter (m) of the pipe section prone to hydrate formation; and v_g is the Velocity (m/s) of the primary continuous gas phase.

Units of interfacial area (A_i) is in m^2. The mass source for Eq. (1), based on Eq. (2), is implemented through a UDF. The mass source is only implemented as a sink for the gas phase, since the formation of hydrates is estimated from the gas consumption rate (Turner et al., 2005).

Momentum Equation:

During the formation of hydrates, the 2-phase flow approximates to an incompressible flow because of increasing gas density and liquid loading, hence the flow is based on the averaging of the flow parameters due to turbulent fluctuations. The Reynolds-Averaged Naiver-Stokes (RANS) momentum equation is as defined in Fluent Theory (2017), below.

$$\frac{\partial}{\partial t}(\overline{\alpha_c}\rho_c\widetilde{u}_c) + \nabla.(\overline{\alpha_c}\rho_c\widetilde{u}_c \otimes \widetilde{u}_c) = -\overline{\alpha_c}\nabla\widetilde{\rho} + \nabla.\overline{\alpha_q}\rho_q\left(\frac{2}{3}k - 2\frac{\mu_{t_q}}{\rho_q}.\nabla.\widetilde{u}_c\right) \tag{6}$$

where the subscripts "c" and "q" represent the carrier (gas) and qth phase respectively. The common interfacial momentum velocity for the formation of hydrates is driven by the velocity of the gas stream (Bendlksen et al., 2004). Hence, the drag force on the primary phase is omitted because the dispersed phase is coupled with the primary phase, and the process is driven by the gas velocity. Wall lubrication by the gas is assumed as "zero" because the pipe wall is wetted by the water phase only. There is also no external body force impacting on the fluid domain. The phase-averaged variables with tilde: $\widetilde{\text{u}}_c$ (averaged velocity) and $\widetilde{\rho}$ (averaged-density) of both phases are defined as:$\widetilde{u}_c = \frac{\overline{\alpha_c \bigcup}}{\overline{\alpha_c}}$ (where $\bigcup$ is the free stream velocity); $\widetilde{\rho} = \frac{\overline{\alpha_c \rho}}{\overline{\alpha_c}}$, where ρ is the free stream density; ρ_c is the density of the gas phase and ρ_q is the density of the qth phase. The turbulent viscosity of the qth phase, μ_{t_q}, is defined in Fluent Theory (2017) as:

$$\mu_{t_q} = \rho_q C_\mu \frac{k_q^2}{\varepsilon_q} \tag{7}$$

where all variables are as defined earlier, and C_μ is the turbulent viscosity constant computed by Fluent for the realizable $k - \varepsilon$ turbulence model, which is adopted in this study as discussed later. The μ_{t_q} links the RANS momentum equation to the turbulence $k - \varepsilon$ transport equations (Eq. (10) & (11)). The lift force on the water droplets on the pipe wall is also neglected because the water is assumed to deposit on the wall as film to form hydrates. Also, it is assumed that the maximum shear stress on the pipe wall by the deposited layer of hydrates, where the wall shedding of the deposited hydrates occurs (Liu et al., 2019).

Energy Equation:

The general form of the energy equation for a multiphase fluid can be written as:

$$\frac{\partial}{\partial t}\left(\alpha_q \rho_q h_q\right) + \nabla.\left(\alpha_q \rho_q \overrightarrow{\vartheta}_q h_q\right) = -\alpha_q \frac{\partial \mathrm{p}_q}{\partial \mathrm{t}} + \tau_q : \nabla \overrightarrow{\vartheta}_q - \nabla.\overrightarrow{q}_q + S_q + \sum_{p=1}^{n}\left(Q_{pq} + \dot{\mathrm{m}}_{pq} h_{pq} - \dot{\mathrm{m}}_{qp} h_{qp}\right) \tag{8}$$

where h_q is the q^{th}phase specific enthalpy; h_{pq} is the interphase enthalpy; S_q is the source energy due to hydrate formation, presented later in Eq. (9); $\overrightarrow{q}_q$ is the heat flux; $\frac{\partial \mathrm{p}_q}{\partial \mathrm{t}}$ is the transient system pressure (Pa/s); and Q_{pq} is the intensity of the heat exchange between the phases (for dispersed secondary phase in a primary phase). The exothermic heat generated is from the formation of hydrate and is implemented in this study as external energy source on the gas phase hence, $Q_{pq} = 0$. With the assumption of no interphase mass transfer, $\dot{\mathrm{m}}_{pq} h_{pq} = 0 \text{ and } \dot{\mathrm{m}}_{qp} h_{qp} = 0$. Other parameters are as defined earlier. The source energy is due to the exothermic hydrate heat of formation. This is given in Meindinyo et al. (2015), as below:

$$S_q = \frac{dm_g}{dt}.\ \Delta H_{Hyd} \tag{9}$$

where $\frac{dm_g}{dt}$ is the gas consumption rate (kg/s) defined in Eq. (2); ΔH_{Hyd} is the enthalpy of hydrate generation (J/kg). The source energy is also implemented in an energy source UDF as a positive driving force only for the gas phase because the dispersed water phase is coupled with the gas phase. Also, there is no slip velocity at the interfacial contact where hydrates are formed.

2.4. Turbulence models

Turbulence models are used extensively in multiphase CFD simulations (Fox, 2014). One of the enabling factors for the formation of hydrate is flow agitation (Carroll, 2014), and it is why hydrate experimental reaction cells are repeatedly stirred to enhance hydrate formation (Aman et al., 2016; Meindinyo et al., 2015). In theory, the right turbulence provides the required interfacial area for the stoichiometric reaction between the reacting species forming hydrates. In this study, the realizable $k-\varepsilon$ two-equation turbulence model was implemented to enhance near wall viscous modelling for predicting hydrate deposition (Wang et al., 2018). Where '*k*' is turbulent kinetic and '*ε*' is turbulent dissipation. The transport equations are solved per phase to account for depositional drift velocity.

Kinetic Equation:

$$\frac{\partial}{\partial t}\left(\alpha_q \rho_q k_q\right) + \nabla.\left(\alpha_q \rho_q \overrightarrow{\vartheta}_q k_q\right) = \nabla.\left(\alpha_q\left(\mu_q + \frac{\mu_{tq}}{\sigma_{\mathrm{kq}}}\right)\nabla k_q\right) + \alpha_q G_{kq} - \alpha_q \rho_q \varepsilon_q + \alpha_q \rho_q \Pi_{kq} \tag{10}$$

Dissipation Equation:

$$\frac{\partial}{\partial t}\left(\alpha_q \rho_q \varepsilon_q\right) + \nabla.\left(\alpha_q \rho_q \overrightarrow{\vartheta}_q \varepsilon_q\right) = \nabla.\left(\alpha_q\left(\mu_q + \frac{\mu_{tq}}{\sigma_{\varepsilon q}}\right)\nabla \varepsilon_q\right) + \alpha_q \frac{\varepsilon_q}{k_q}\left(C_{1\varepsilon} G_{kq} - C_{2\varepsilon} \rho_q \varepsilon_q\right) + \alpha_q \rho_q \Pi_{\varepsilon q} \tag{11}$$

where Π_{kq} and $\Pi_{\varepsilon q}$ are source terms for the turbulence interactions between the entrained water phase and the primary gas phase; G_{kq} is the turbulent kinetic energy production term per qth phase; μ_{tq} is the turbulent viscosity (Pa.s) of the qth phase. Buoyancy effect and fluctuating dilatation have been neglected in Eq. (10), because the flow is incompressible. For the current work, both equations are solved per phase to enhance the prediction of hydrates at the wall. $C_{1\varepsilon}$ $C_{2\varepsilon}$ and $C_{3\varepsilon}$ are constants. The terms σ_{kq} and $\sigma_{\varepsilon q}$ are the turbulent kinetic energy (TKE) and turbulent dissipation rate (TDR) Prandtl numbers and ascribed constant values of 1 and 1.2, respectively as recommended in the literature (Fluent Theory, 2017). Both σ_{kq} and $\sigma_{\varepsilon q}$ relates to the dimensionless ratio of the temperature-dependent kinematic eddy viscosity of the continuous gas phase to the dispersed liquid phase. The value of σ_{kq} has been set to ensure that the ratio of momentum diffusivity to thermal diffusivity equals to "1," because thermal diffusivity from the gas phase to the liquid phase at the wall should be balanced by the velocity of the carrier phase during the formation of hydrates to enhance hydrate stability and reduce advection (Tu et al., 2018). For the realizable $k-\varepsilon$ model, $C_{1\varepsilon}$ is calculated by the software during the simulation. The values for the constants used in this study are: $C_{2\varepsilon}(1.9)$ and $C_{3\varepsilon}(1.3)$. In addition, the closure parameters $\Pi_{kq}$and $\Pi_{\varepsilon q}$ are achieved per phase using the closure model by Simonin and Viollet (1990), as modified in Fluent Theory (2017):

For the primary continuous phase:

$$\text{Kinetic source}: \ \Pi_{kq} = C_s \alpha_q K_{pq} \overrightarrow{v}_{pq}.\overrightarrow{v}_{dr} \tag{12}$$

$$\text{Dissipation source}: \ \Pi_{\varepsilon q} = C_{3\varepsilon}\frac{\varepsilon_k}{k_q}\Pi_{kq} \tag{13}$$

For the dispersed secondary phase:

$$\text{Kinetic source}: \ \Pi_{kp} = C_s \alpha_p K_{pq} \overrightarrow{v}_{pq}.\overrightarrow{v}_{dr} \tag{14}$$

$$\text{Dissipation source}: \ \Pi_{\varepsilon p} = C_{3\varepsilon}\frac{\varepsilon_k}{k_p}\Pi_{kp} \tag{15}$$

where the constants $C_{3\varepsilon} = 1.3$ and $C_s = 1$; K_{pq} is the covariance of the phase velocities; $\overrightarrow{v}_{dr}$ is drift velocity between the gas and liquid phase; $\overrightarrow{v}_{pq}$ is the relative velocity between both phases. The drift velocity is calculated from the relation proposed by Simonin and Viollet (1990) as follows:

$$\overrightarrow{v}_{dr} = -\frac{D_{t,pq}}{\sigma_{pq}}\left(\frac{\nabla_{\alpha_p}}{\alpha_p} - \frac{\nabla_{\alpha_q}}{\alpha_q}\right) \tag{16}$$

where $D_{t,pq}$ represent the binary diffusivity ($D_{t,pq} = \frac{1}{3}K_{pq}\tau_{t,pq}$); $\tau_{t,pq}$ is the eddy particle interaction time; ∇_{α_p} and ∇_{α_q} are the variations in concentration of the gas and liquid phase respectively; σ_{pq} is the dispersion Prandtl number, usually set to 0.75 to increase thermal diffusivity in incompressible flow. However, turbulent dissipation force is set to "none" for all simulations in this study to limit the conversion of kinetic energy into thermal internal energy. Again, the dissipation term can be neglected in incompressible flow when there is need to prevent flow induced mechanical deformation of a viscous fluid, which is the case in predicting hydrates deposition (Tu et al., 2018).

2.5. Wall shear stress

The turbulent stress τ_c^t on the hydrates at the pipe wall is governed by the carrier (gas) phase and defined from the stress term on the right-hand side (RHS) of Eq. (6) as:

$$\tau_c^t = \overline{\alpha_c}\rho_c\left(\frac{2}{3}k - 2\frac{\mu_{t_c}}{\rho_c}.\nabla.\widetilde{u}_c\right) \tag{17}$$

The parameters in Eq. (17) retain their previous definitions.

2.6. Enhanced near wall effects

2.6.1. Pressure gradient effect

The near wall pressure predictions can be unreliable due to boundary layer separations when the pipe wall is subjected to severe pressure gradients as a result of turbulence (Mottaghian et al., 2018). This can occur during hydrate deposition on the wall since the surface of the hydrate layer creates a wavy stratified annular profile (Aman et al., 2016; Di Lorenzo et al., 2018), hence the need to ensure the Reynolds number is in the transition zone by preventing turbulent dispersion as explained earlier. The effect of turbulence on near wall pressure predictions is minimised by enhanced wall treatment with the pressure gradient effects activated under realizable $k-\varepsilon$ turbulence model in ANSYS Fluent.

2.6.2. Thermal effect

Hydrate deposition is dependent on thermal gradient between the fluid and the pipe wall (Turner et al., 2005). Near wall turbulence affects the thermal profile (Kader, 1981). Also, with increasing thermodynamic mixing (Abbasi and Hashim, 2014), there is a reduction in the temperature of the gas at the core, leading to further hydrates generation. Hence, to solve the near wall thermal heat transfer accurately, there is the need to consider the varying near wall eddy viscosity. As the hydrates profile grows, the near wall thermal effect also varies (Aman et al., 2016; Di Lorenzo et al., 2018). Thus, the lower turbulent kinetic energy Prandtl number of 1 used in the simulations was done to enhance the stability of hydrates on the wall of the pipe by enhancing the thermal cooling of the gas. Consequently, thermal effect was activated as enhanced wall treatment on the realizable $k-\varepsilon$ turbulence model in this study.

2.7. Mesh grid sensitivity analysis

The computational geometry is 3D representation of a 10 m length and 0.0204 m diameter pipe. This diameter is the same used in the experimental setups, where the generation of hydrates occurs at a 12 m section of the experimental flowloop (Aman et al., 2018). The use of 10 m length CFD model was premised on the fact that hydrates are produced at a section of the pipeline and transported downstream where it plugs bends or areas of constriction as indicated in the flowloop experiments (Aman et al., 2016, 2018; Di Lorenzo et al., 2014b). Also, pipelines can span lengths of up to 100 km and above, which is difficult to model using CFD because of computer processing time. As a result, it was important to ascertain if a shorter length than the 34 m used in the above experimental setups can accurately predict the deposition rates of hydrates and flow behaviour, especially when the hydrates were generated in a 12 m section of the test flowloop. Flow materials are methane gas and water, with defined properties in the literature (Di Lorenzo et al., 2018). Inlet velocities range from 2.0 m/s to 8.8 m/s at various sub-cooling temperatures ranging from 2.5 K to 8.0 K. To enhance multiphase flow in the oil and gas industry, pipelines are designed to reduce the pressure drop by minimising friction loss and pipewall erosion. Hence, the stability of the CFD simulation was improved by choosing a mesh size with the least significant pressure drop through a mesh grid sensitivity analysis in Fig. 4. The mesh sensitivity was carried out at the inlet velocity of 10 m/s (flowrate of 3.3 kg/s), temperature of 292 K, and pressure of 8.8 MPa.

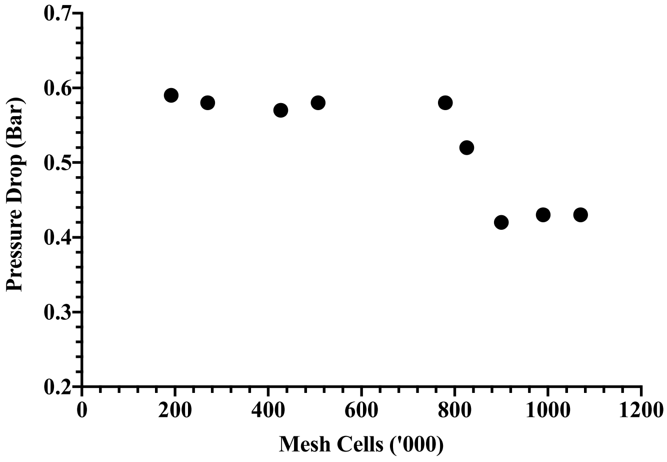

Fig. 4. Mesh sensitivity.

From Fig. 4, the mesh size of 900,000 cells resulted in the lowest pressure-drop of 0.42 bar and was selected as the model mesh size. The effect of the mass and energy source UDFs on the primary phase using this grid size is presented in Fig. 5, below. Implying that the UDF codes resulted in shorter flowtime. Also, the slight increase in pressure at 8.8 m/s on the UDF curve in Fig. 5 is due to accurately metered gas mass flowrate based on the kinetics model. Without the UDFs, the software underpredicted the deposition rates of hydrates and extended the simulation flowtime.

The flow behaviour captured by the pressure profile indicates that the UDF codes resulted in a better prediction of hydrate deposition, as higher pressure drop indicate higher risk of hydrate blockage (Lv et al., 2012). The UDF codes also incorporated a conditional statement using Eq. (18), as proposed by Sloan and Koh, 2007 for methane hydrates at 0 to 25 °C to calculate the resulting equivalent system pressure at the hydrate formation temperature. The peak pressure at 3.0 s indicates full agglomeration of hydrates filling the pipe annulus, and the drop in pressure after 3.0 s represent the deposition of hydrates, allowing for ease of fluid flow at the core until the line is plugged with hydrates beyond 3.8 s.

$$P_{eq} = exp\left(38.98 - \frac{8534}{T_{eq}}\right) \tag{18}$$

where P_{eq} is the hydrate formation equilibrium pressure (KPa). This calculated equivalent pressure must be equal or less than the system pressure for the hydrates to be stable in the pipeline because hydrate formation and stability is favoured at high pressure and low temperature. The fluid properties and input parameters for the simulations are presented in Tables 1–4 below.

The Peng and Robinson equation of state (EOS) is used to calculate gas density (Table 1), as it is widely used in gas pipeline hydraulic calculations, because the equation expresses the compositional properties of natural gas in terms of both critical properties and acentric factor (Peng and Robinson, 1976). Also, the gas viscosity and heat capacity were calculated by the kinetic theory to account for the effect of turbulence on the system thermodynamics. During simulation, the pipeline temperature in the fluid domain is reduced from the inlet value of 292 K by the subcooling temperature at the pipe wall to lower temperatures favouring hydrate formation and stability, as indicated in Fig. 11, and the temperature contour maps (Fig. 15 and Fig. 16).

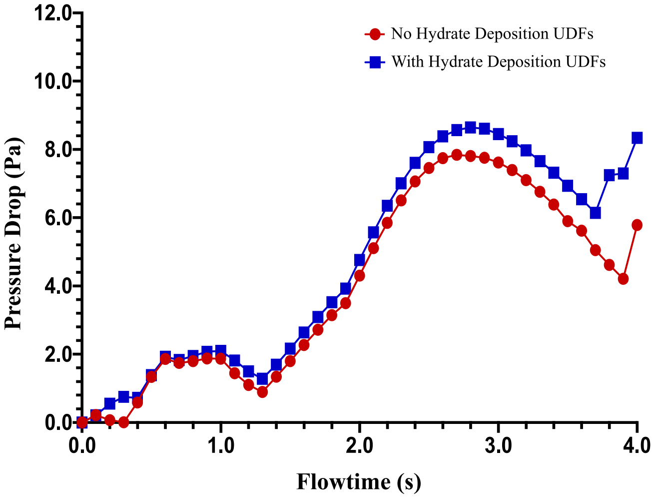

Fig. 5. Comparison of pressure drop (with and without hydrate deposition UDFs) at gas flow velocity of 8.8 m/s.

Table 1
Natural gas properties (Ansys Fluent Version 2020 R1).

Natural Gas Properties	Value
Gas density (kgm^{-3})	Peng Robinson (real gas)
Molecular weight of natural gas (kg.kmol^{-1})[a]	18.043
Viscosity (Pa.s)	Kinetic theory
Thermal conductivity (W.m^{-1}K^{-1})	0.0332
Constant pressure heat capacity (J$\cdot$K^{-1}kg^{-1})	Kinetic theory
Critical pressure (MPa)	4.6
Critical temperature (K)	191
Critical specific volume (m^3/kg)	6.15×10^{-3}
Reference temperature (K)	298.15
Energy parameter (k)	148.6
Degrees of freedom	0
Characteristics length (angstrom)	3.758
Standard state enthalpy (J.kg^{-1}mol^{-1})	-7.49×10^{-7}
Standard state entropy (J.kg^{-1}mol^{-1})	1.86×10^{5}
Acentric factor	0.01

[a] *Gas molecular weight from Di Lorenzo et al. (2018), based on the gas composition.*

Table 2
Liquid water properties (Ansys Fluent Version 2020 R1).

Liquid Water Properties	Value
Water density (kgm^{-3})	998.2
Molecular weight (kg.kmol^{-1})	18.0152
Viscosity (Pa.s)	1.0×10^{-3}
Thermal conductivity (W.m^{-1}K^{-1})	0.626
Constant pressure heat capacity (J$\cdot$K^{-1}kg^{-1})	4182
Interfacial tension with gas phase (N$\cdot$m^{-1})	0.0721
Standard state enthalpy (J.kg^{-1}mol^{-1})	-2.858×10^{8}
Reference temperature (K)	298

Table 3
Gas hydrate properties.

Gas Hydrate Properties	Value
Hydrate density (kgm^{-3})[a]	807.77
Hydrate enthalpy of formation (Jkg^{-1})[b]	6.4×10^{5}

[a] (Balakin et al., 2016).
[b] (Di Lorenzo et al., 2018).

Table 4
Input parameters/boundary conditions (Di Lorenzo et al., 2018).

Input Variables	Value
Velocity (m/s)	4.7; 8.8
Inlet operating pressure (MPa)	8.8
Inlet operating temperature (K)	292
Inlet water volume fraction	0.06
Pipe wall temperature (K)	Operating temperature less subcooling temperature
Pipe internal wall surface roughness (dimensionless)[a]	0 (Smooth pipe)
Gauge pressure (Pa)	101,325

[a] (Jassim et al., 2010).

2.8. Fluent solver configuration

Pressure-based fluent solver is activated to combine the continuity and momentum equation. Such that, in the discretization of mass conservation equation when the velocity gradient is already derived from the momentum equation at the cell centre, there is also implicit incorporation of the resultant pressures at the cell centres (Ashrafizadeh et al., 2015; Vakilipour et al., 2019). The “$k - \varepsilon$” turbulent equation was set to realizable to ensure the positivity of normal stresses when the strain rate is large as suggested by Shih et al. (1995), because of near-wall turbulent shear stress effect. Also, activating thermal effects enables the modelling of the thermal transfer on the near-wall viscous layer between the fluid and pipe wall based on the subcooling temperature gradient, which is important in hydrates deposition rates prediction (Lim et al., 2020; Turner et al., 2005).

2.9. Solution method

The solution method is Phase coupled SIMPLE to avoid instabilities because of the incompressible nature of the flow and the pressure build up during phase change; especially for transient time-dependent problems where computer CPU time is a concern for convergence (Fluent Theory, 2017). Here, due to pressure-velocity coupling, the pressure and velocity are stored at cell centres (Ferreira et al., 2019). Relaxation factor is set to 0.75. Under-relaxation factors were set to appropriate values for the simulation, as they suppresses the oscillations between timesteps so that convergence is achieved (Barron and Neyshabouri, 2003). For optimum result, both pressure under-relaxation factor (φ_p) and velocity under-relaxation factor ($\varphi_{\mathscr{U}}$) must sum up to 1 and it was ensured that $\varphi_{\mathscr{U}} > \varphi_p$ (Demirdzic et al., 1987; Min and Tao, 2007). Gradient is set to Least Square Cell Based (LSCB), because it is time saving and can achieve a minimum of first order accuracy (Mishriky and Walsh, 2017). Furthermore, pressure is solved through second order upwind scheme, thus providing a better accuracy through multidimensional linear reconstruction (Shyy et al., 1992). Also, cell face fluxes for solved parameters are cell-averaged values and assumed to hold for all cells (Ferreira et al., 2019). At the outlet, the “radial equilibrium pressure distribution” option was activated to further enhance annular hydrate deposition prediction, because hydrates are deposited on the wall by radial velocity (Wang et al., 2018). Backflow is not anticipated since it is a continuous pipeline with exit. However, for incompressible flows the timesteps was not considered as a major criterion for convergence because it is not limited by Courant Friedrich Levy (CFL) criterion in implicit functions (Bendlksen et al., 2004). The CFD software solved six equations: mass, momentum, volume fraction, energy, turbulence (kinetic and dissipation) and interfacial area concentration. Calculation for each case was achieved for 4.0 s with fixed time advancement, 40 time steps and time step size of 0.1 s. The simulation was achieved with a computer of 2.10 GHz quad-core Intel Xeon Gold 6230 CPU and RAM size of 16 GB. The results, validation and discussions are presented in section 3.0.

3. Results, validation and discussion-

The empirical results of this CFD model at 4.7 m/s and 8.8 m/s predicted within ±10% uncertainty bound of the quantile-quantile slope plots (Fig. 7 and Fig. 8) for both experimental results (Aman et al., 2016; Di Lorenzo et al., 2014a) and analytical model results (Di Lorenzo et al., 2018). At lower gas velocity of 4.7 m/s, the model overpredicted the hydrates deposition rates of the experimental results in Aman et al. (2016) by 9–25.7%, whereas the analytical model of Di Lorenzo et al. (2018) underpredicted the same experimental results by a range of 27–33% (Fig. 9). Consequently, the CFD model can improve proactive hydrate plugging risk predictions earlier than the analytical model. Similarly, at a velocity of 8.8 m/s and subcooling temperatures of 2.5 K, 7.1 K and 8.0 K, the CFD model underpredicted the hydrate deposition rates of the regressed experimental results in Di Lorenzo et al. (2014a) by 14%, 6% and 4% respectively, and overpredicted the results by 1% at a subcooling temperature of 4.3 K (Fig. 10). In comparison, the hydrate deposition rate predictions of the analytical model in Di Lorenzo et al. (2018) at a velocity of 8.8 m/s and increasing subcooling temperatures were inconsistent with theorized linear regression trend, as the model prediction at the subcooling temperature of 2.5 K was higher than subsequent predictions at higher subcooling temperatures (Table 6). Finally, the CFD model predicted the locations and corresponding phase change during hydrate formation, agglomeration, and deposition.

Especially, the CFD model also captured hydrate formation, agglomeration, deposition and plugging through pressure and temperature curves as reported in the literature (Liu et al., 2020). Under similar subcooling temperature (e.g., 4.5/4.3), doubling the velocity also doubles the deposition rate, which is also consistent with the experimental report in Aman et al. (2016). From the mode results we suggest that hydrate sloughing shear stress is relatively constant, and the wall shedding shear stress by hydrates vary during deposition. Again, in all the temperature contour maps generated (Figs. 15–17), there is a reducing temperature profile towards the wall and the annular flow pattern observed is consistent with experimental visual observations (e.g., Ding et al., 2017; Di Lorenzo et al., 2014b). The gas density also increases from the pipe core towards the wall (Fig. 19), which also resonates with reported experimental observations (Di Lorenzo et al., 2014b; Aman et al., 2016; Ding et al., 2017). All simulations were carried out within the temperature and pressure corridor for the experimental observations of Di Lorenzo et al. (2014a, b) and Aman et al. (2016) as shown in the hydrate loci curve in Fig. 6. Thus, confirming that the CFD results presented in detail hereafter predicted the formation and deposition of hydrates.

As indicated in Fig. 6, at the system inlet operating pressure of 8.8 MPa, the stability of hydrates is at temperatures lower or equal to 290 K. The simulation is temperature driven, with the hydrates equivalent pressure computed from Eq. (18). Gas cooling occurs at the pipewall, hence increasing the density of gas (Fig. 19). This also influence the gas flow rate in the fluid domain. The measured gas flowrate is determined using a UDF code based on Eq. (2), with variables defined and explained in Eqs. (3)–(5). The measured gas flow rate in the fluid domain mimicked the formation, agglomeration, and deposition of hydrates in the fluid domain (Fig. 12). Also, this study assumed a linearly growing annular profile of hydrates deposits on the pipe wall to account for linear reduction in pipeline hydraulic diameter based on the temperature profile along the pipe. The adopted profile of hydrates deposition on the pipe wall is based on observed experimental annular-dispersed pattern during hydrate formation and deposition (Aman et al., 2016). Thus, the morphology of spatial nucleation and deposition of hydrates is outside the scope of this study. The details of the model validation are discussed in section 3.1.

3.1. CFD model validation

In this section, the predicted deposition rates of hydrates are validated with both experimental and analytical results in the subsections that follows.

3.1.1. Hydrate deposition rates

The deposition rate results have been validated with both experimental (Aman et al., 2016; Di Lorenzo et al., 2014a) and analytical results (Di Lorenzo et al., 2018) in Table 5 and Table 6. The average deposition rates of hydrates for all subcooling temperatures from Fig. 24 and Fig. 25 are computed during hydrates deposition as indicated in section III of Fig. 12, identified as first average deposition rate. In Figs. 7 and 8, the graphical comparison of the predicted deposition rates by the CFD model with experimental and analytical results are presented. Aman et al. (2016) mentioned the presence of uncertainties in the estimated deposition rates of hydrates in their experiment at 4.6 m/s. For instance, at gas velocity of 4.6 m/s and subcooling temperature of 7.0 K, Aman et al. (2016) reported 0.004 L/min as the average hydrates

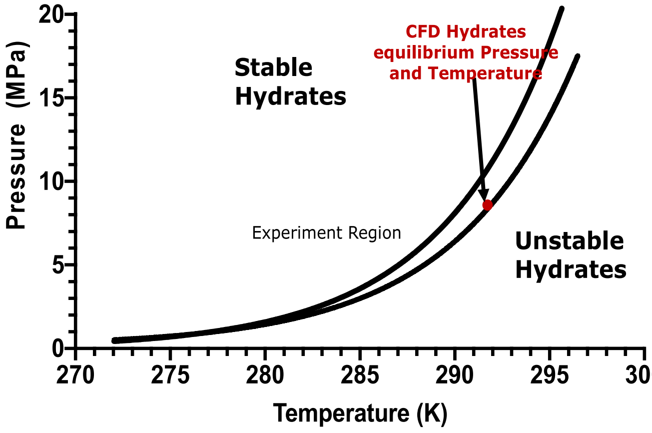

Fig. 6. Methane hydrate loci showing experimental region.

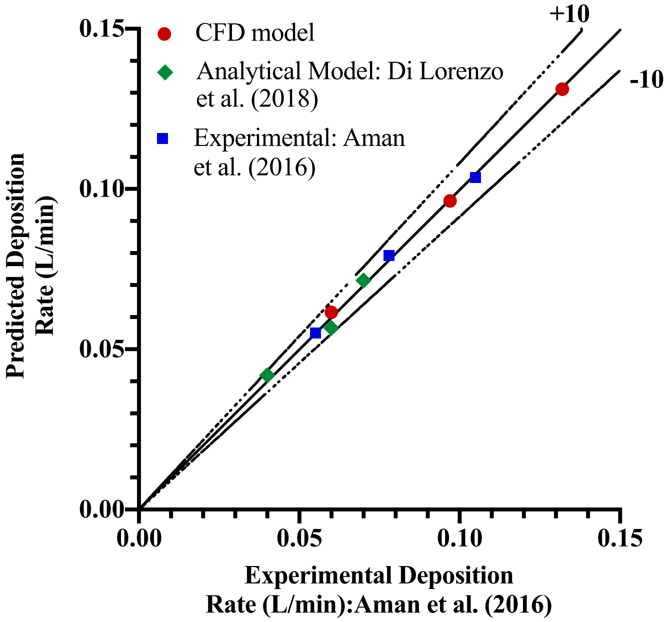

Fig. 7. 10% bound Q-Q plot comparison of CFD model prediction of hydrate deposition rates at a gas velocity of 4.7 m/s with experimental and analytical model results.

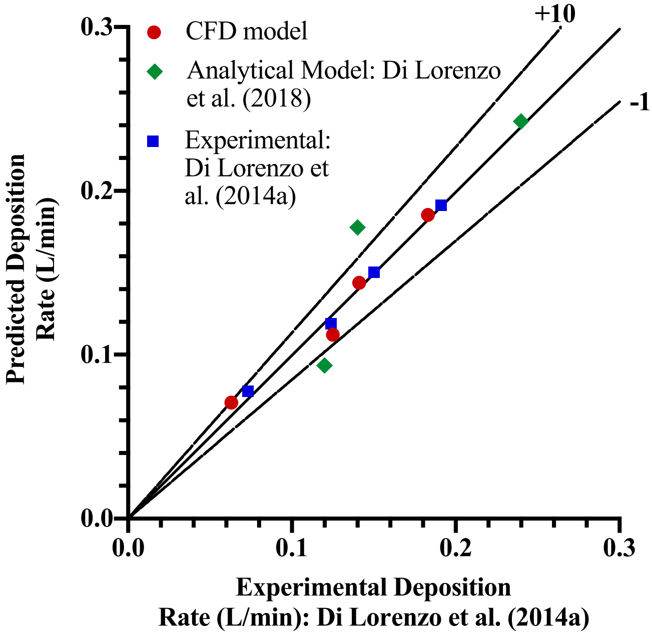

Fig. 8. 10% bound Q-Q plot comparison of CFD model prediction of hydrates deposition rates at a gas velocity of 8.8 m/s with experimental and analytical model results.

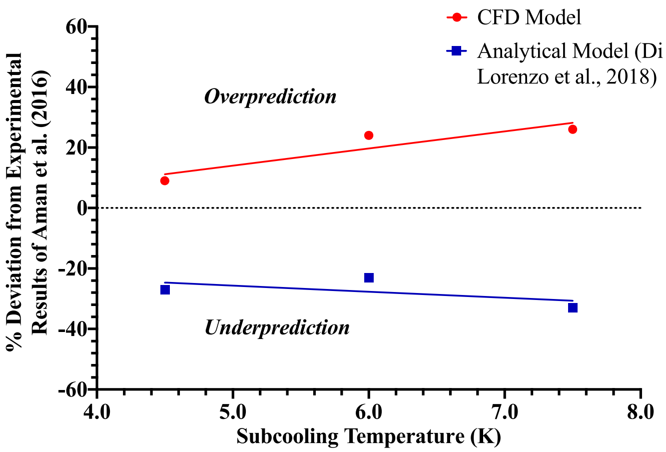

Fig. 9. Comparing % deviation from experimental results at gas velocity of 4.7 m/s.

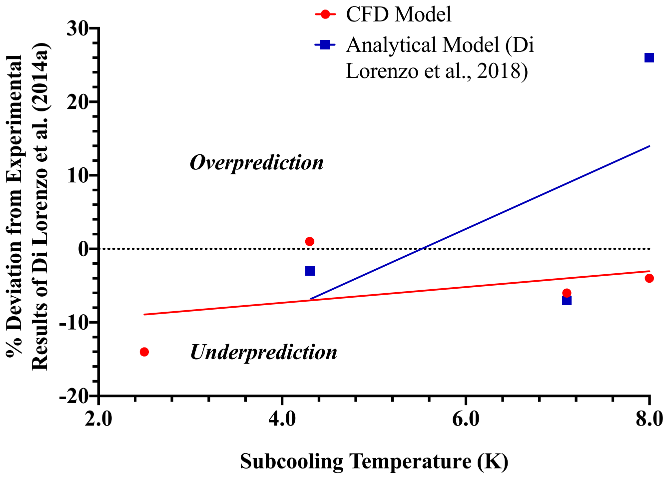

Fig. 10. Comparing % deviation from experimental results at gas velocity of 8.8 m/s.

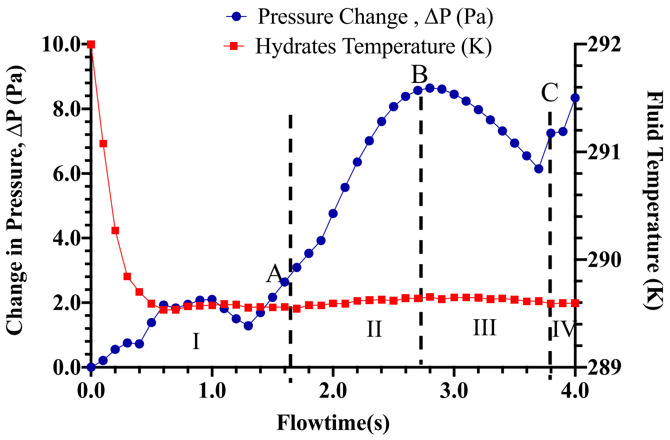

Fig. 11. Relationship between pressure and temperature variation at 8.8 m/s and subcooling temperature of 7.0 K.

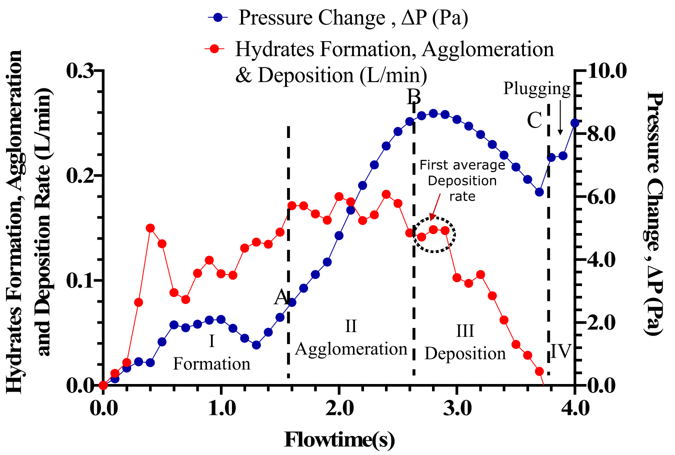

Fig. 12. Relationship between pressure drop and hydrate deposition rate at 8.8 m/s and subcooling temperature of 7.0 K.

Table 5
Hydrate deposition rate validation at 4.7 m/s.

Velocity (m/s)	Sub-Cooling Temp.(K)	Average Hydrate Deposition Rate (L/min)		
		Aman et al. (2016) (Exp.)	Di Lorenzo et al. (2018) (Analytical)	CFD Model
4.7	4.5	0.055	0.04	0.060
	6.0	0.078	0.06	0.097
	7.0	0.004^a	0.07	0.121
	7.5	0.105	0.07	0.132

[a] Experimental data considered an outlier because it did not agree with the expected outcome of higher deposition rate as subcooling temperature increases.

Table 6
Hydrate deposition rate validation at 8.8 m/s.

Velocity (m/s)	Sub-Cooling Temp.(K)	Average Hydrate Deposition Rate (L/min)		
		Di Lorenzo et al. (2014a) (Exp.)^a	Di Lorenzo et al. (2018) (Analytical)	CFD Model
8.8	2.5	0.073	0.34††	0.063
	4.3	0.124	0.12	0.125
	7.1	0.150	0.14	0.141
	8.0	0.191	0.24	0.183

[a] The experimental deposition rates are regressed from the uninhibited results in Di Lorenzo et al. (2014a) at subcooling temperatures of 4.5 K, 4.7 K, 6.8 K and 8.8 K. †† Analytical data was considered an outlier because it dd not agree with the expected outcome of lower deposition rate as subcooling temperature reduces.

deposition rate. Since hydrates deposition increases with subcooling temperature, this value was considered an outlier and not included in the graph for Aman et al. (2016) in Fig. 7 below. Also, at 8.8 m/s and a subcooling temperature of 2.5 K, the analytical model of Di Lorenzo et al. (2018) predicted a value of 0.34 L/min and followed with lower values as the subcooling temperatures increased. As a result, this value was considered an outlier because it did not represent the theorized regression trend of lower deposition rate as subcooling temperature reduces.

As indicated in Tables 5 and 6, the hydrate deposition rate values obtained by this CFD model compared favourably with both experimental and analytical results. Again, the CFD simulated hydrate deposition rate of 0.125 L/min at 8.8 m/s and 4.3 K compared favourably with 0.15 L/min reported in the analytical model of Wang et al. (2018). For similar lower subcooling temperatures (e.g., 4.5 K/4.3 K) doubling the velocity also doubled the deposition rate of hydrates. As the subcooling temperature increased, this effect also reduced; for instance, doubling the velocity at subcooling temperature of 7.0 K/7.1 K only increased the deposition rate by approximately 16.5%. Implying that subcooling temperatures plays a significant role in hydrates plugging risk prediction. The quantile-quantile (Q-Q) plot in Figs. 7 and 8 below compares the CFD model result with both experimental and analytical hydrate deposition rates within 90% confidence interval, to investigate the consistency of the results predicted by the CFD model across the subcooling temperatures.

The dotted linear lines in Figs. 7 and 8, represent the consistency of the CFD model predictions within ±10% uncertainty bound compared with experimental and analytical results. The deviation of the CFD model predictions from experimental results is discussed further. The observation from Table 5, suggests that the CFD model at low gas velocity of 4.7 m/s is a better alternative compared to the analytical model. At lower velocity of 4.7 m/s (Fig. 9), the CFD model results overpredicted the experimental results by a range of 9–25.7%, whereas the analytical model of Di Lorenzo et al. (2018) underpredicted the same experimental results by a range of 27–33%. Hence, the risk of underpredicted hydrate plugging risk is expected using the analytical model, especially at higher subcooling temperatures and lower gas velocity. In practice this can occur in under-capacity utilization flow regime in gas pipelines.

As seen from Fig. 9, the predictions of the CFD model at low gas velocity can lead to a proactive hydrates control intervention under low gas productivity, while the predictions from the analytical model can lead to delayed intervention with attendant pipeline failure risk from overpressurisation.

Furthermore, at a higher velocity of 8.8 m/s the regressed experimental data in Table 6 at subcooling temperatures of 2.5 K, 7.1 K and 8.0 K were underpredicted by the CFD model by 14%, 6% and 4% respectively (Fig. 10). Also, the CFD model overpredicted the same experimental results by 1% at a subcooling temperature of 4.3 K. However, aside the hydrate deposition rate prediction by the analytical model of 0.34 L/min against the regressed experimental value of 0.073 L/min at the subcooling temperature of 2.5 K in Table 6, the hydrate deposition rate predictions of the analytical model indicates underprediction of experimental results by 3% and 7% at subcooling temperatures of 4.3 K and 7.1 K respectively and overpredicted the same experimental results by 26% at the subcooling temperature of 8.0 K, which is appropriate for a proactive hydrate deposition rate predicting model. From the linear trend in Fig. 10, there is the tendency that the CFD model will overpredict the experimental hydrate deposition rates as the subcooling temperatures increases beyond 8.0 K. The risk of hydrate plugging is reduced at higher gas velocity (Aman et al., 2016), hence, the observation from the results (Table 6 and Fig. 10) indicates that the predictions from the CFD model is a consistent linear representation of the theorized positive regression trend of increasing hydrate deposition rates as the subcooling temperatures increases at constant gas velocity.

Therefore, the outcomes of the validation above implies that the CFD model prediction is more proactive in hydrates plugging risk prediction, and an improvement over the predictions by the analytical model of (Di Lorenzo et al., 2018) at simulation conditions of low gas velocity. At higher velocities of 8.8 m/s, the predictions of both models are relatively the same except at lower subcooling temperatures of 2.5 K where the analytical model prediction was not consistent with expected reduction in the deposition rates of hydrates compared with values obtained at higher subcooling temperatures.

Figs. 11 and 12 below presents the graphical representations of the relationship between hydrate formation, agglomeration, and deposition rates, fluid temperature and pressure drop, and are used to describe the process of phase change in hydrate-forming gas pipeline (Fig. 29). From Fig. 11, the hydrates were stable after a flowtime of 0.3 s. It has been observed that viscosity increases during the agglomeration of hydrates (Bbosa et al., 2019). Consequently, the increasing resistance to flow because of increase in viscosity also lead to increase in pressure drop (Di Lorenzo et al., 2014b). The descriptions and indications observed in all the simulations compare favourably with experimental observations, as discussed further.

In Figs. 11 and 12, hydrate formation, agglomeration, deposition and pipe plugging are represented in sections I, II, III and IV respectively as indicated in (Liu et al., 2020). Higher hydrates formation risks are possible in gas-dominant pipelines because of lower volume fraction of liquid water (Sloan et al., 2011b). The formation and agglomeration of hydrates are characterised by phase change and can be measured by the gas flowrate in the fluid domain. Experimental results suggest an increase in gas flowrate during hydrate formation because of the increase in gas consumption rate (Odutola et al., 2017; Turner et al., 2005). Also, the gas flowrate is relatively stable during agglomeration (Odutola et al., 2017) and decreases during hydrates deposition because of reduction in pipe hydraulic diameter (Aman et al., 2016). The transient pressure drop was superimposed on the hydrate curve in Fig. 12 to explain the effect of these stages on the pressure drop in the pipeline. As discussed later in section 3.6 (Fig. 29), hydrate formation and agglomeration in gas-dominant pipeline occur during 3-phase flow of gas, water, and hydrates (section I) and 2-phase flow of gas and hydrates (section II), respectively. Consequently, the formation of hydrates is not possible in section II, because of the absence of water in the fluid domain. The rates of hydrate formation, agglomeration and deposition are indicated on the left-hand side of the vertical axis in Fig. 12, and can be obtained from the curve. Full agglomeration of hydrates was achieved in stage II at an average rate of 0.17 L/min in Fig. 12. The temperature in Fig. 11 is relatively stable during full agglomeration of hydrates (section II), hydrate deposition (section III) and pipe plugging (section IV), which is similar to indications in the literature (Li et al., 2013; Liu et al., 2020; Odutola et al., 2017; Turner and Talley, 2008). In section III, the gradually decline in deposition rate is consistent with observations in literature (Liu et al., 2019). Also evident from the graph is the sharp rise in the system pressure during the agglomeration of hydrates, which is also consistent with experimental observations (e.g., Di Lorenzo et al., 2014a; Aman et al., 2016). By comparing the transient temperature curves at subcooling temperature of 7.0 K at gas velocities of 4.7 m/s and 8.8 m/s (Fig. 13), the observation suggests that hydrates are more stable at lower flow velocities. This observation is consistent with indications in the literature (Aman et al., 2016).

The indication in Fig. 13 explains why the plugging of pipelines by hydrates is severe at low gas velocities. Whereas the deposition rates of hydrates increases at higher gas velocities under similar subcooling temperatures (Aman et al., 2016), the increase in gas velocity enhances the interaction of the hydrates at the wall with the gas at the core, thus increasing the near wall temperature at the velocity of 8.8 m/s. This explains why there are lower sloughing of hydrates events at low flow velocity (Aman et al., 2016). Hydrates were unstable at the core as indicated from the temperature profile in Fig. 14.

Details of the results from the CFD model simulations are discussed further in sections 3.2 to 3.9.

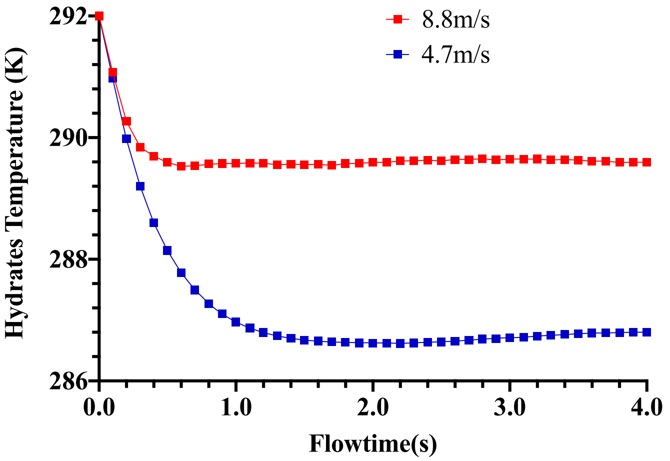

Fig. 13. Comparing hydrate temperatures at subcooling temperature of 7.0 K with gas flow velocities of 4.7 m/s and 8.8 m/s.

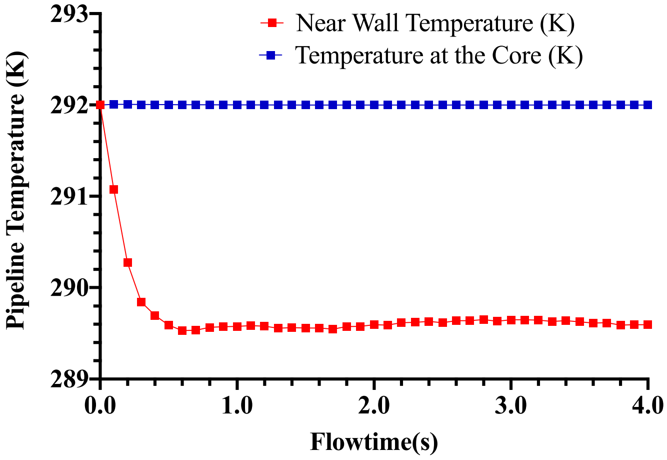

Fig. 14. Comparing the stability of hydrate near the pipe wall and at the core at subcooling temperature of 7.0 K with gas flow velocity of 8.8 m/s.

3.2. Temperature contours showing the effect of changes in velocity and subcooling temperatures during hydrate deposition

The temperature contours in Figs. 15–17, represent the thermal behaviour of hydrate formation because of the temperature-dependent solubility of the gas in water. By varying the gas velocity while keeping the subcooling temperature constant at 7.0 K, 2D cross-sectional slices of gas temperature contour maps along the horizontal section of the pipe are obtained and presented in Fig. 15. From the contour maps with a cut-off minimum temperature of 287.6 K for the purpose of comparison, annular layers of temperature variations indicates that the temperature at the pipe wall is lower than that at the core. Severe cases of hydrate deposition in the pipeline occurs at lower gas velocities (e.g., 2.0 m/s) and higher subcooling temperatures (e.g., 7.0 K). Also indicated in Fig. 15 is a tapering effect of the gas core along the pipe and from bottom (highest velocity) to top (lowest velocity) for the range of flow velocities simulated. The diameter of the gas at the core at the temperature of 292 K indicates availability of gas for the formation and sloughing of hydrates. A reduction in gas volume and quality also occurs as the gas core reduces along the pipe due to hydrate formation and deposition. As a result, the gas-water-hydrate flow during the formation of hydrates is relatively incompressible. Also, from Fig. 15 a comparison of the profiles at gas velocities of 2.0–8.0 m/s explains the effect of increasing velocity on the depositional distance of hydrates (Jassim et al., 2010).

Although more hydrates are formed at higher velocities of 6.0 m/s and 8.0 m/s due to the increase turbulence of dispersed water droplets (Aman et al., 2016) and the increased solubility of gas, the hydrates are deposited farther downstream of the point of hydrate nucleation (Jassim et al., 2010). Thus, higher velocities increase hydrate loading into the continuous gas phase, until the gas is totally consumed in the water phase to form hydrates. Again, the variation of temperature across the 2D cross-sectional slices at constant velocity was investigated as shown in Fig. 16, to explain the thermal effect of varying the subcooling temperature at constant flow gas velocity on hydrate formation and deposition.

The contour maps in Fig. 16 suggests increasing hydrate formation and deposition as the subcooling temperature increases. This indication provides insight into the behaviour of gas flow in hydrate-forming pipelines during temperature changes from summer to winter, for instance. This can also occur when the thermal integrity of the external pipe insulation is compromised and allows the conduction of the ambient temperature in an offshore environment across the wall of the pipe to the fluid domain.

From both Figs. 15 and 16, it is advisable to investigate the optimum velocity that can decrease the concentration of hydrates (Yongchao et al., 2019), without adversely compromising gas quality and transportability, especially during seasonal temperature changes. One clear inference from Figs. 15 and 16, is the tapering effect observed along the pipeline from the inlet as indicated in Fig. 17 below, which can lead to plugging of the horizontal section or riser base of subsea pipelines with hydrates (Aman et al., 2018).

The pattern in Fig. 17, agrees with experimental observations in the literature. The tapering effect shows that hydrates will eventually plug the pipeline at a distance from the inlet. Again, the presence of hydrates as dispersed phase in the gas phase is possible because of the dispersed water phase in the gas stream in Fig. 18. The higher gas temperature of 292 K indicates that the hydrates at the core will not be stable until the entire gas is consumed. From Fig. 18, the water phase maximum temperature of 290 K will continue to enhance the cooling of the gas for more stability of hydrates, since the gas temperature of 292 K is already at the hydrate equilibrium temperature point. Eventually, the pipe core will be filled with hydrates once the entire gas is consumed.

3.3. Gas density contours showing cross-sectional increase in gas density towards the wall of the pipe

A cross-sectional density profile at the subcooling temperature of 7.0 K and velocities of 4.7 m/s and 8.8 m/s, indicates how the gas density varies across the section in a reducing core phenomenon (Fig. 19). This observation is consistent across all the subcooling temperatures simulated.

The higher gas density at the wall is because methane solubility in water increases at lower temperatures (Lekvam and Bishnoi, 1997). This phenomenon is also related to hydrate formation and deposition. With increase in density, gas compressibility reduces, and the flow become increasingly viscous resulting in increasing pressure drop.

3.4. Pressure drop during hydrate formation, agglomeration and deposition with change in velocity and subcooling temperature

Transient pressure drop graphs can provide insight into how change in velocity and subcooling temperatures affects hydrates-induced flow hydraulics in gas pipelines. The effect of varying flow velocity on

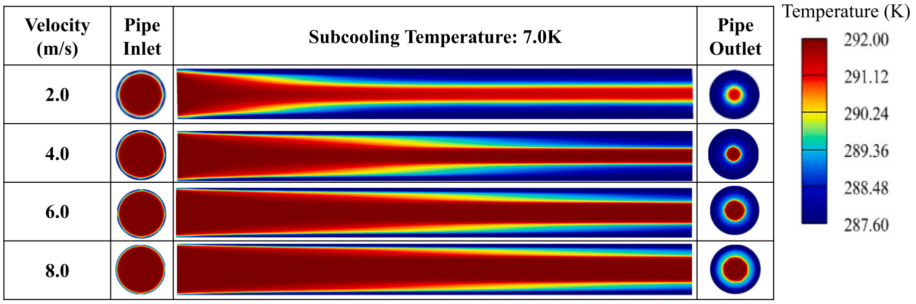

Fig. 15. Temperature contour at varying velocities and constant subcooling temperature of 7.0 K for the gas phase.

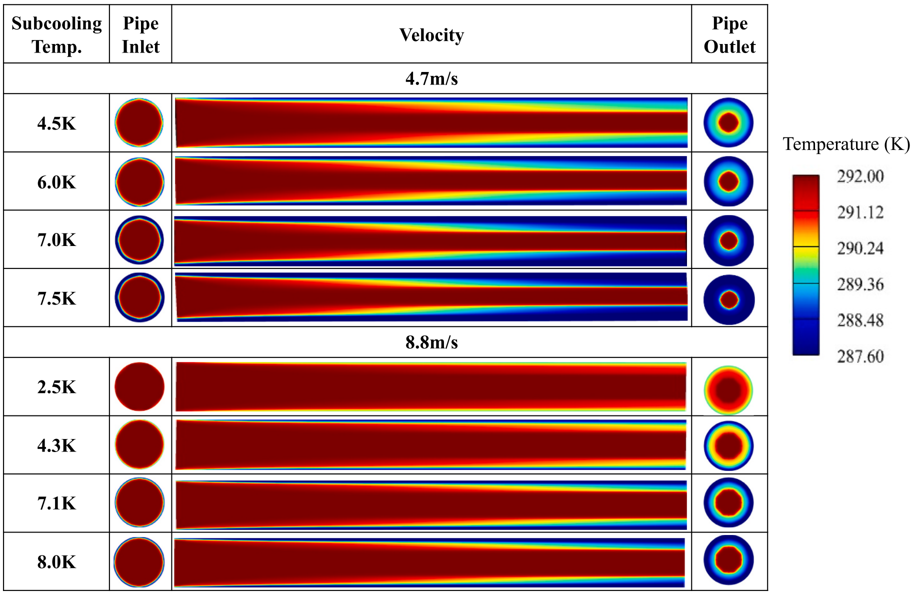

Fig. 16. Temperature contour at varying subcooling temperatures and constant velocities of 4.7 m/s and 8.8 m/s for the gas phase.

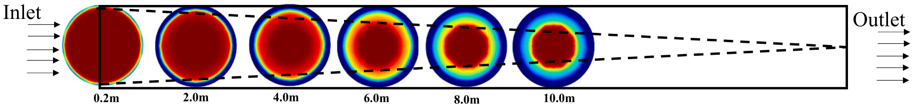

Fig. 17. Temperature contour tapering effect of hydrate deposition along the pipe at a velocity of 8.8 m/s and subcooling temperature of 7.1 K.

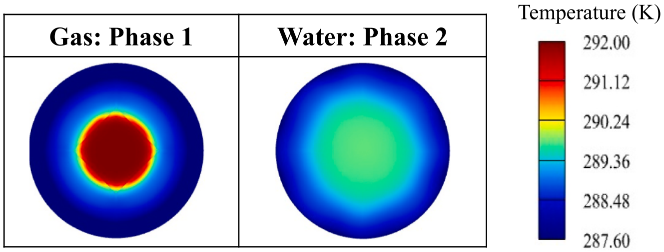

Fig. 18. Temperature contours of gas and water phase at gas velocity of 8.8 m/s and subcooling temperature of 7.1 K indicating the formation of Hydrates as dispersed phase and deposition on the wall of the pipe.

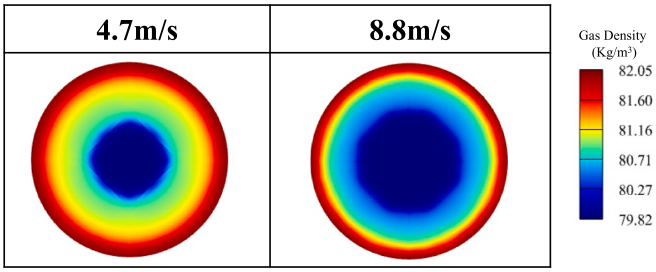

Fig. 19. Gas density contour increasing towards the wall of the pipe at subcooling temperature of 7.0 K.

pressure drop during the CFD simulation is presented in Fig. 20.

From Fig. 20, at a subcooling temperature of 4.5 K and same pressure drop, for instance, the simulation at a velocity of 8.8 m/s attained pressure drop value of 9.0 Pa at 2.9 s earlier than the simulation at 4.7 m/s which attained this same transient pressure drop of 9.0 Pa at 3.9 s. This observation is similar with the empirical remark by Aman et al. (2016) - that the experimental time to attain the maximum transient pressure drop of the flowloop facility was shorter at higher velocity than at lower velocity. The practical implication of this indication is that hydrates plugging risk should be anticipated earlier at higher gas velocity, especially at the riser base. Following the observations in Figs. 11 and 12 discussed earlier, the two dips on the pressure curves in both plots at subcooling temperatures of 4.5 K and 7.0 K at 8.8 m/s in Fig. 20 indicates the onset of the agglomeration of hydrates (first dip), and the second dip is hydrates deposition. Also, for both velocities the maximum pressure-drop observed at 7.0 K is greater than that at 4.5 K for the same flowtime. As seen in Fig. 20 above, the transient pressure drop increases as the velocity increases because of increase in hydrate formation by the increasing turbulence in the pipeline.

In Fig. 21, it is observed that increase in subcooling temperatures did not imply a significant increase in the transient pressure drop along the pipe at constant velocity, which also agrees with experimental observations. At a constant gas velocity of 4.6 m/s, Aman et al. (2016) observed similar behaviour from their experiments.

Furthermore, the extended position of the second dip at both subcooling temperatures in Fig. 21, implies increased hydrates deposition rate when the gas velocity was increased from 4.7 m/s to 8.8 m/s.

3.5. *Quantitative measurement of hydrate deposition rates*

The hydrate deposition graphs presented in this section are based on the mass of gas flow rate in the fluid domain, as a representation of the gas consumption rate during hydrate formation, agglomeration and deposition discussed earlier. A sample plot of the gas flowrate versus the simulation flowtime at 8.8 m/s and 7.0 K subcooling without UDF is presented in Fig. 22, below.

Turner et al. (2005) suggests that the formation of hydrates is instantaneous at the right subcooling temperature. Also, hydrate deposition velocity is assumed to be constant for a fully developed turbulent flow in the pipeline (Jassim et al., 2010). Therefore, the average gas

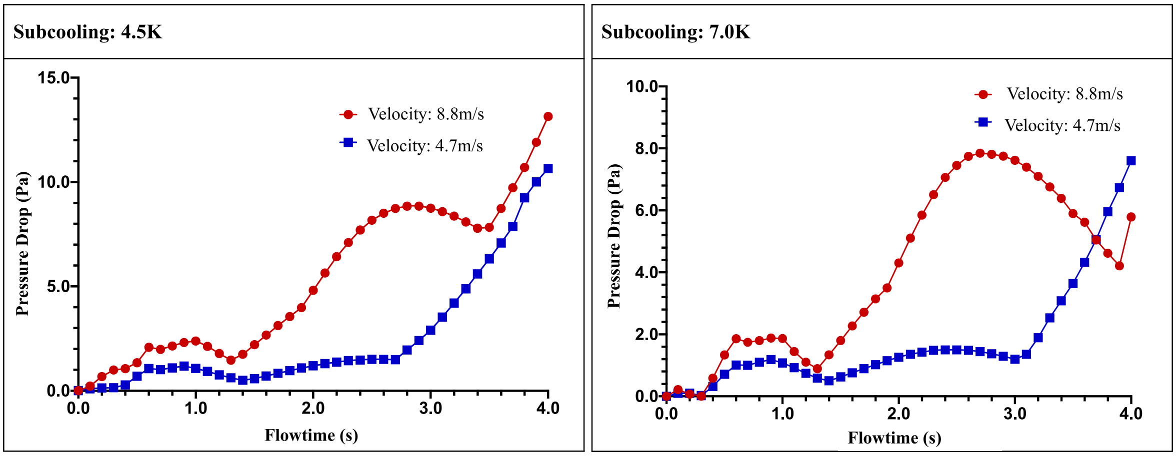

Fig. 20. Effect of velocity change under constant subcooling temperature on pressure drop during hydrate formation, agglomeration, and deposition.

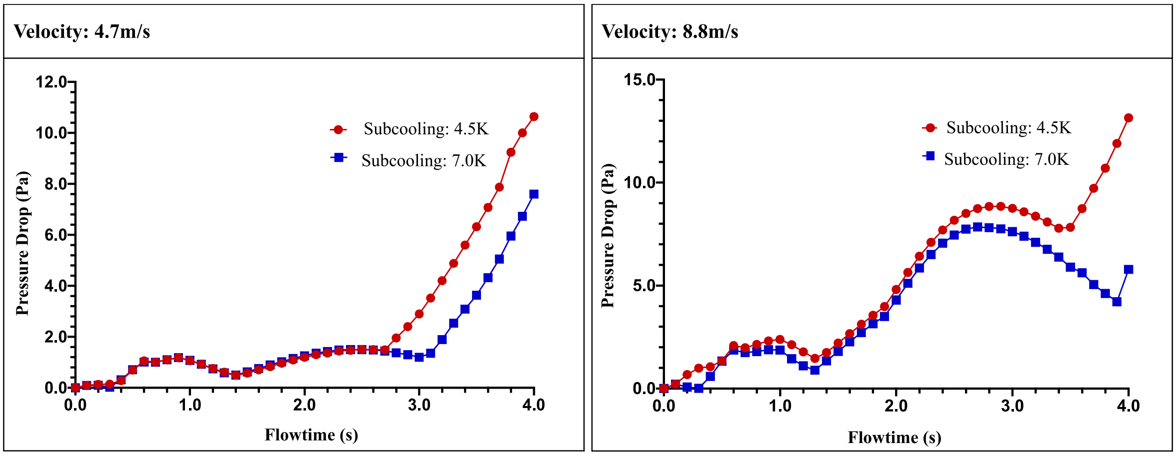

Fig. 21. Effect of change in subcooling temperature at constant velocity on pressure drop during hydrate formation, agglomeration, and deposition.

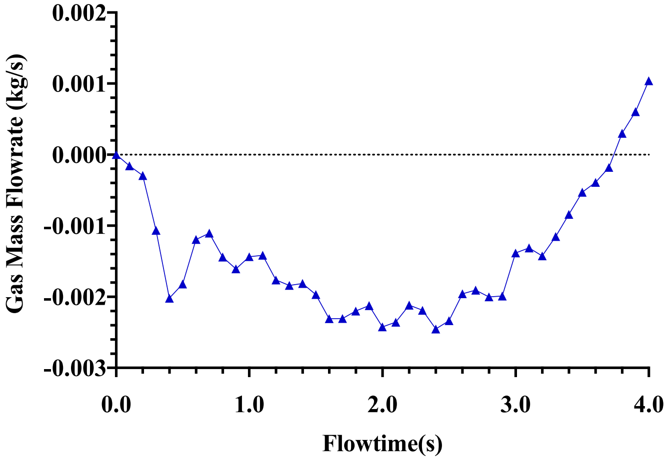

Fig. 22. Gas mass flowrate during hydrate formation, agglomeration, and deposition.

consumption rate (kg/s) is expected to be the best approximation of hydrate deposition (Aman et al., 2016; Di Lorenzo et al., 2014b; Liu et al., 2019; Turner et al., 2005). Based on the eulerian-eulerian model and the assumption of no interphase mass transfer, the right-hand side of Eq. (1), reduces to the mass source term S_q only, which is implemented in a gas injection UDF. The energy source term in Eq. (9), is also implemented in another UDF. The plot for both UDF and no UDF simulation at a velocity of 8.8 m/s and subcooling temperature of 7.1 K are compared in Fig. 23, below.

As indicated in Fig. 23, ANSYS Fluent can produce similar gas mass flowrate results without the UDFs for a model length of 10.0 m, provided the boundary conditions for the formation of hydrates are the same. For

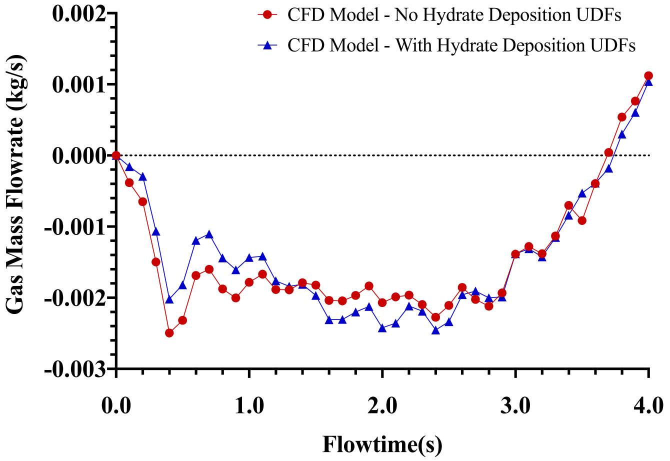

Fig. 23. Comparison of gas mass flowrate ‘with’ and ‘without’ hydrate deposition UDFs.

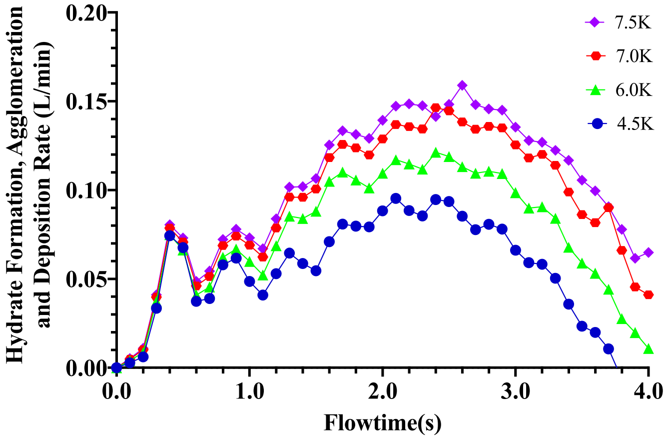

Fig. 24. Comparing hydrate deposition curves at a velocity of 4.7 m/s for various subcooling temperatures.

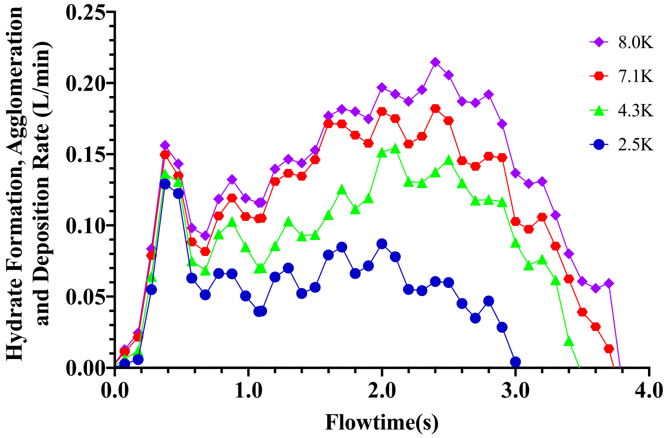

Fig. 25. Comparing hydrate deposition curves at a velocity of 8.8 m/s for various subcooling temperatures.

the UDFs curve, the initial gas consumption rate was lower up to 1.1 s but increased slightly thereafter until 2.6 s. From this point both curves reduced gas mass flow rates along the same curve. Moreover, while the non-UDFs curve maintained a seemingly stable horizontal profile during the hydrate agglomeration period (1.0–2.8 s), the UDF curve maintained a non-uniform trough with a vertical dip at 2.0 s within this same period. The implementation of the UDF codes in this research is to ensure that the energy source term is based on experimental correlations in Eq. (9), and the make-up gas supplied into the domain is in the same proportion with empirical predictions in Eq. (19). The hydrate deposition rates in Figs. 24–26 are estimated from Eq. (19), below.

$$Q_{H\_d} = \frac{-60000\dot{m}_{CH_4}}{\rho_{H\_hwc}} \tag{19}$$

where Q_{H_d} is hydrate deposition rate, L/min; $\dot{m}_{CH_4}$ is gas mass flowrate, kg/s; ρ_{H_hwc} is the density of hydrate (807.77 kg/m^3) from Table 3. For validation, the recorded hydrate formation data at 4.7 m/s and 8.8 m/s are plotted for different subcooling temperature simulations and presented hereafter in Figs. 24 and 25. The comparisons indicate an increasing the deposition rate of hydrates as the subcooling temperature increases. This is because of the increased solubility of methane gas in water at lower temperatures below the hydrate formation condition (Lekvam and Bishnoi, 1997).

The UDFs simulated hydrate curves in Figs. 24 and 25 attains a hydrate agglomeration/growth rate peak before a deposition (decline point on the curves). The simulated deposition rates as indicated in stage III of Fig. 12 are computed from Eq. (19) and presented in Table 7 below.

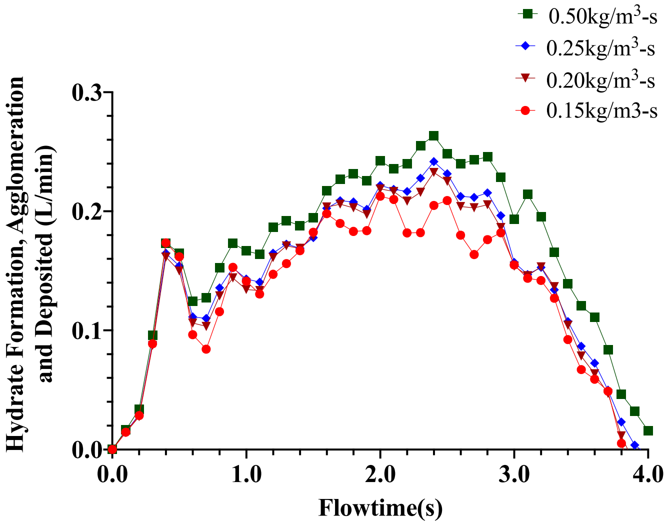

Fig. 26. Comparing hydrate formation for various gas supply rate at a velocity of 8.8 m/s and constant subcooling temperature of 8.0 K.

In Table 7, at 4.7 m/s and 8.8 m/s for all subcooling temperatures there is an increasing trend of hydrate deposition rates as the subcooling temperature increases. This trend is due to methane solubility as explained earlier, hence deposition rate of hydrates is positively related with subcooling temperatures. This observation agrees with experimental report in Aman et al. (2016), that hydrates deposition rate is positively influenced by increase in velocity.

To estimate the deposition rates of hydrates at different gas flowrates, the gas flowrates are entered as constant negative source mass for the gas phase. So that the CFD software compute the added flowrates as externally controlled gas input into the control system. Fig. 26 indicates the effect of injecting various gas mass flowrate per volume into the system on hydrate deposition at 8.8 m/s and subcooling of 8.0 K.

The results in Fig. 26 indicate that increasing the gas supply into the system increases hydrate deposition rates, provided the conditions for the formation of hydrates are met. This observation is important in managing hydrates. Furthermore, as gas supply is cut off, the growth of hydrates is also stopped (Neto et al., 2016). In operations and maintenance, once hydrates start forming in a pipeline, the first technical advice is to stop the flow of gas (Li et al., 2013). Again, if hydrates deposition rates are estimated during design, the operations of hydrate-forming pipelines can be optimised based on routine cleaning operations and maintenance planning. It is also important to estimate the equivalent gas supply rate to the rate of hydrates deposited by superimposing the graph at 8.8 m/s and 8.0 K subcooling temperature in Fig. 25 on Fig. 26 as presented in Fig. 27.

From Fig. 27, the relationship between gas consumption rate and hydrate deposition rate was set at: 0.183 L/min (black curve) of hydrates deposited is equivalent to 0.2 kg/m^3-s of gas injected. Implying that 1.1

Table 7
Model predicted hydrate deposition rates.

Velocity (m/s)	Sub-Cooling temp.(K)	CFD Model Predicted Average Hydrate Deposited Rate (L/min)
4.7	4.5	0.060
	6.0	0.097
	7.0	0.121
	7.5	0.132
8.8	2.5	0.063
	4.3	0.125
	7.1	0.141
	8.0	0.183

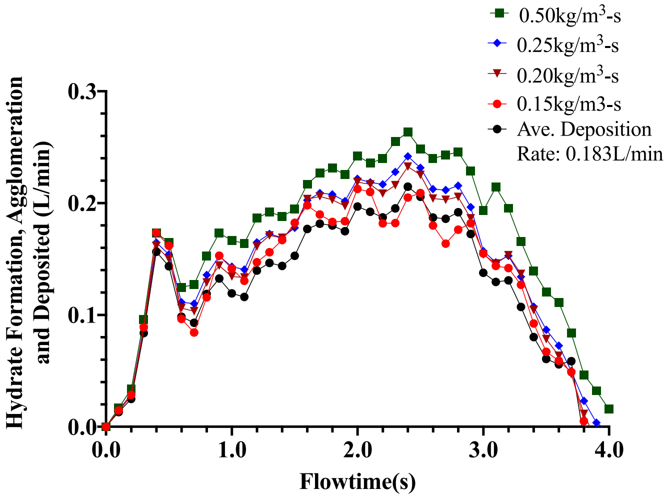

Fig. 27. Estimating the relationship between hydrate deposition rate and gas supply rate at a velocity of 8.8 m/s and subcooling temperature of 8.0 K.

kg/m^3-s of consumed gas deposited 1 L/min of hydrates. Again, at lower velocity of 4.7 m/s and subcooling temperature of 7.0 K, this relationship also holds (Fig. 28). Thus, by converting to mol/min of gas supplied based on the volume of the pipe and molecular weight of the gas (Table 1), it is estimated that 12 mol/min of gas deposited 1 L/min of hydrates. The above indication shows that gas availability in the pipeline is the determining factor for hydrate formation and deposition.

3.6. Effect of hydrates on volume fraction of gas and water

The sum of the volume fractions is equal to 1. The volume fraction of gas and water will reduce during hydrate formation. Hydrate volume fraction α_h, was estimated by subtracting the sum of the minimum transient volume fraction of gas and water from 1 (Eq. (21)).

$$\sum \alpha_q = 1 \tag{20}$$

$$\alpha_h = 1 - (\alpha_g + \alpha_w) \tag{21}$$

where α_q, the volume fraction of each phase and subscripts, g, w, and h represent gas, water, and hydrate phase respectively. From 2.0 s of flowtime, both gas and water phase formed a viscous flow that mimicked the flow of hydrate slurry in gas pipeline.

The volume fractions in Fig. 29, are the minimum values obtained in the fluid domain of the pipe section. This was appropriate to ensure that the values computed by the software was representative of reality. As indicated in Fig. 29, the transient multiphase flow phase change during hydrate formation, agglomeration and deposition are: (i) 2-phase flow of water and gas between 0.0 s and 0.1 s; (ii) 3-phase flow of gas, water, and hydrates between 0.1 s and 1.0 s; (iii) 2-phase flow of gas and hydrates between 1.0 s and 1.9 s; and (iv) agglomeration and deposition of hydrates beyond the flowtime of 1.9 s–4.0 s. At full occlusion, the volume fraction of water ranges from 0.000029 to 0.0000011 respectively, whereas the volume fraction of gas beyond the flowtime of 1.9 s was already "zero." This insignificant volume fraction of water after the expiration of the gas phase beyond 1.9 s indicates the presence of slight hydrates slurry (agglomeration) and high deposition on the wall, which led to a drop in transient pressure between the flowtime of 2.8 s and 3.8 s (Fig. 11). This is because, as the hydrates were deposited on the wall, there was a slight increase in hydraulic diameter for the light hydrate slurry to flow. Later in Fig. 33, it will be noticed that the tangential velocity of the hydrates slowed down, implying a gradual reduction in deposition as more hydrates are deposited on the wall. However, not all the hydrates are stable as the temperature of the hydrates at the core is 290 K (Fig. 18). As indicated earlier in Figs. 11 and 12, agglomeration occurred after 1.0 s. The inlet temperature of 292 K was reduced to hydrate-forming temperature in 0.1 s (Fig. 11). This observation is supported in the literature (Turner et al., 2005), that the formation of hydrates is instantaneous at the right subcooling temperature. Again, the observation of 3-phase flow (gas, water, and hydrates) followed by 2-phase flow (hydrates and gas) in Fig. 29 is consistent with the suggestion in the literature (Wang et al., 2018). The plugging risk of Hydrates increases at lower near wall temperatures as indicated by the hydrate volume fraction (Fig. 30), hence at lower gas flow velocity hydrate plugging risk is higher in agreement with earlier indications in Fig. 13.

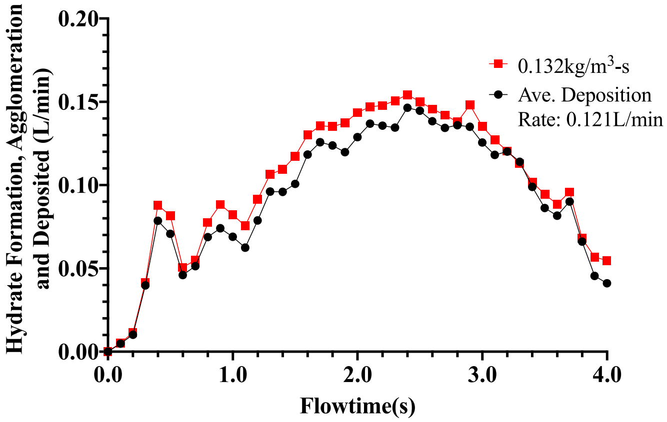

Fig. 28. Estimating the relationship between hydrate deposition rate and gas supply rate at a velocity of 4.7 m/s and subcooling temperature of 7.0 K.

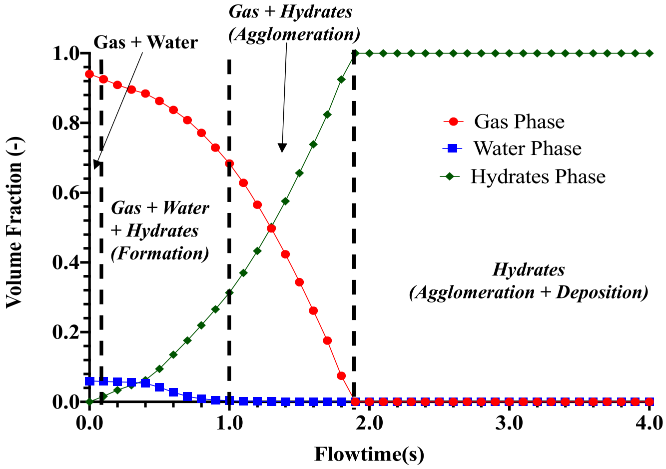

Fig. 29. Phase change during hydrate formation, agglomeration, and deposition at gas velocity of 8.8 m/s and subcooling temperature of 7.0 K.

A decrease in the deposition rates of hydrates was observed when the water volume fraction was increased (Fig. 31). Implying that reducing the water volume fraction leads to decrease in liquid loading by the carrier phase and increases hydrate plugging risk. This observation is also corroborated in another study (Chaudhari et al., 2018). Increase in water volume fraction also encourages the sloughing of hydrates (Di Lorenzo et al., 2014b).

3.7. Effect of turbulence and tangential velocity on hydrate deposition

The deposition of hydrates is controlled by the source mass in Eq. (1). From Eq. (1), the source mass is expected to be the dependent variable. Since the gas phase is treated as sink, with increase in gas density towards the wall because of the subcooling temperature at the wall, the

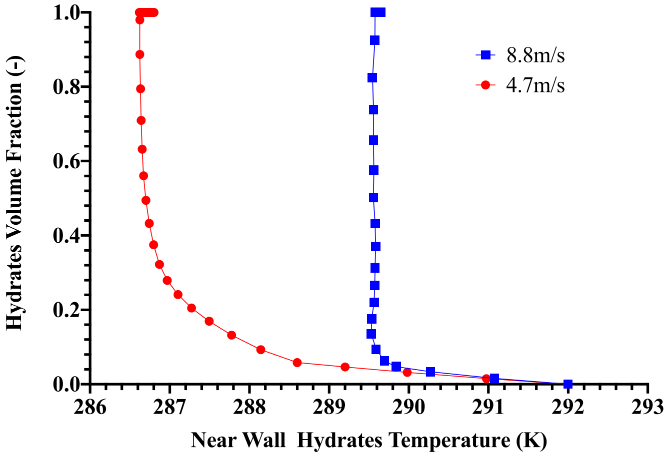

Fig. 30. Effect of temperature on hydrate plugging risk at subcooling temperature of 7.0 K.

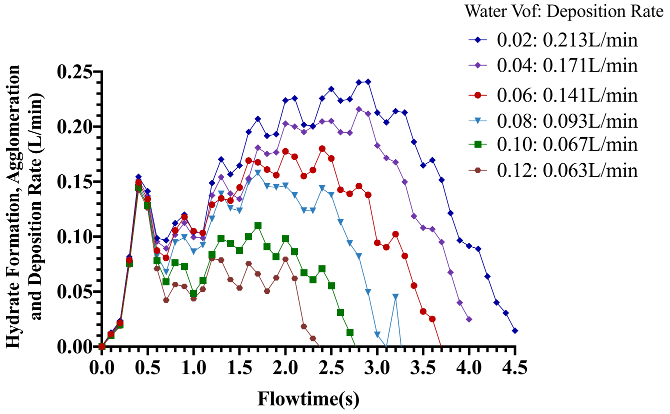

Fig. 31. Effect of water volume fraction on hydrate deposition rates at subcooling temperature of 7.0 K and gas velocity of 8.8 m/s.

only variable that will adjust to accommodate the mass flowrate of the injected gas based on the law of mass conservation is the gas velocity. Hydrate deposition is favoured in laminar and transition flow regimes. Hence, the velocity of the gas and water will reduce under the above scenario. Laminar flow occurs in the pipeline if the turbulent Reynolds number is less than 2100, and turbulent, if the Reynolds number is greater than 4000 (Munson et al., 1994). Between these two values, the flow is transitional, implying switch between laminar and turbulent flow. Turbulence is present at the gas-liquid interface (Di Lorenzo et al., 2014a), and enhances hydrate formation. The turbulent Reynolds number, Re_y (Fluent Theory, 2017) is given as:

$$Re_y = \frac{\rho y \sqrt{k}}{\mu} \tag{22}$$

where y is the distance to the nearest wall (m); ρ, is the density of the fluid domain (kg/m^3); k, is turbulent kinetic energy per unit mass (J/kg); and μ, is the fluid viscosity (Pa.s). The Re_y value explains the flow in the viscosity-affected-near-wall region (Fluent Theory, 2017), and important here because the deposition of hydrates is a near-wall phenomenon. From Eq. (22), increasing the viscosity of hydrates reduces the Reynolds number as the density is relatively stable (Ding et al., 2017; Li et al., 2013). Hence, the Re_y represent the Reynolds number of hydrates in the pipe. The curves in Fig. 32, are plots of maximum turbulent Reynolds number, Re_y, at the subcooling temperature of 7.0 K and gas velocities of 4.7 m/s and 8.8 m/s.

Both simulations at 4.7 m/s and 8.8 m/s are within the transition flow zone during agglomeration and deposition. The higher turbulence at the Re_y values of 4000–6000, enabled good temperature mixing leading to the formation of hydrates. During the transition flow, hydrates deposition is enhanced. The tangential velocity of hydrates also enhances hydrates agglomeration in readiness for deposition (Fig. 33). The agglomeration of hydrates commenced at 1.0 s and deposition commenced at 2.8 s as discussed earlier in Figs. 11 and 12. At 4.7 m/s, the hydrates remained in the gas phase until 2.0 s before drifting towards the wall when the flow was relatively steady (Fig. 32). At higher gas velocity, the hydrates tangential velocity is higher, implying a much farther depositional distance as seen in the temperature contour profile at 8.8 m/s and subcooling temperature of 7.0 K in Fig. 15.

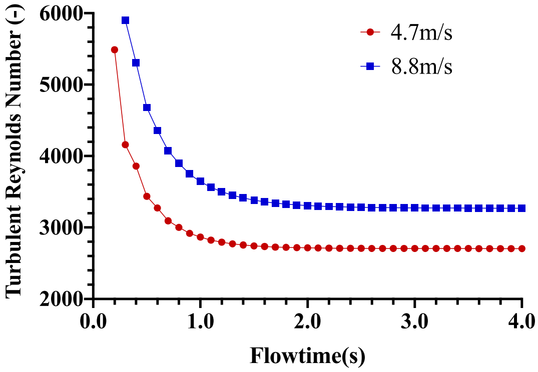

Fig. 32. Effect of hydrate formation, agglomeration, and deposition on turbulent Reynolds number at subcooling temperature of 7.0 K.

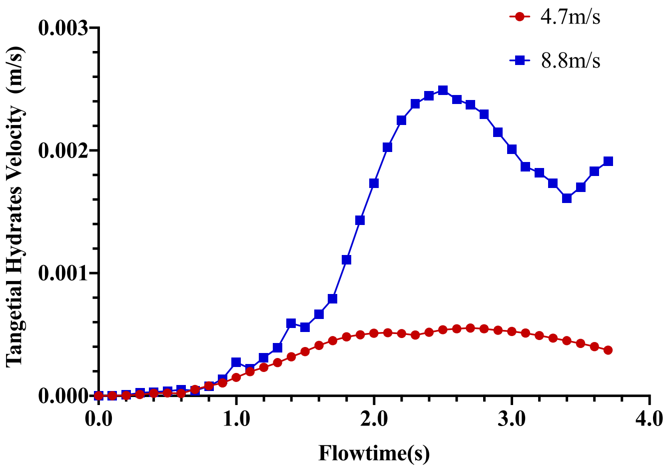

Fig. 33. Tangential velocity of hydrates at subcooling temperature of 7.0 K.

During agglomeration (1.0 s–2.8 s), the tangential velocity increases and drop during deposition between 2.8 s and 3.5 s at both 4.7 m/s and 8.8 m/s. At 3.4 s and velocity of 8.8 m/s, the tangential velocity started rising because more hydrates are depositing.

3.8. Effect of pipe length on hydrate deposition rate

Two model lengths of 10 m and 1 m and same pipe diameter of 0.0204 m were simulated in this analysis. The inlet and outlet surfaces of the pipe were meshed to the same mesh cells. The results are presented in Table 8.

The indications in Table 8, is that the 1.0 m length did not agree with the expected increasing trend of hydrate deposition rates as subcooling temperature increases at the higher velocity of 8.8 m/s. This is because the entry length for this diameter is 0.612 m resulting in a highly unstable flow in the 1 m length pipe at 8.8 m/s. Thus, substantiating the

Table 8
Comparison of hydrate deposition rates for CFD model lengths.

Velocity (m/s)	Sub-Cooling temp.(K)	Average Hydrate Deposited Rate (L/min)	
		CFD Model (1.0 m length)	CFD Model (10.0 m length)
4.7	4.5	0.058	0.060
	6.0	0.065	0.097
	7.0	0.072	0.121
	7.5	0.071	0.132
8.8	2.5	0.151	0.063
	4.3	0.133	0.125
	7.1	0.133	0.141
	8.0	0.117	0.183

use of a higher length of 10 m for this study.

3.9. *Effect of pipe diameter on hydrate deposition rate*

This sensitivity investigates the need of developing new horizontal geometry with changing diameter and mesh sizes for each flow case when the pipe diameter varies. The hydrates deposition rates at a velocity of 8.8 m/s and subcooling temperature of 7.1 K are plotted for pipe dimeters of 0.0204 m, 0.0408 m and 0.0612 m in Fig. 34. The outcome is represented in a linear relationship in Fig. 35 for the purpose of deriving a linear mathematical relation that can aid in the extrapolation of the deposition rates of hydrates for any diameter of pipe.

Fig. 34 shows that increasing the pipe diameter also increases the rates of hydrates deposition because of increase in gas volume. The hydrate deposition rates in L/min for each pipe diameter were plotted in Fig. 35, below.

Thus, as indicated in Fig. 35, increasing the pipe diameter at the same velocity and subcooling temperature increases the volume of gas, which is a determining factor in hydrate formation and deposition. Also, increase in pipe diameter imply increase in the volume of free water. The observation in Fig. 35 is supported by Aman et al. (2016), that increase in the amount of entrained water increases hydrate formation and deposition. From the linear graph in Fig. 35, a relationship between the deposition rate of hydrates and pipe diameter is stated as:

$$Q_{h\_d} = 9.075D \tag{23}$$

where Q_{h_d} retains the earlier definition in Eq. (23). Therefore, the corresponding diameter can be written as:

$$D = \frac{Q_{h\_d}}{9.075} \tag{24}$$

To find the approximate hydrate deposition rate for a higher diameter by extrapolation, we can use the ratio of the pipeline diameters as shown below:

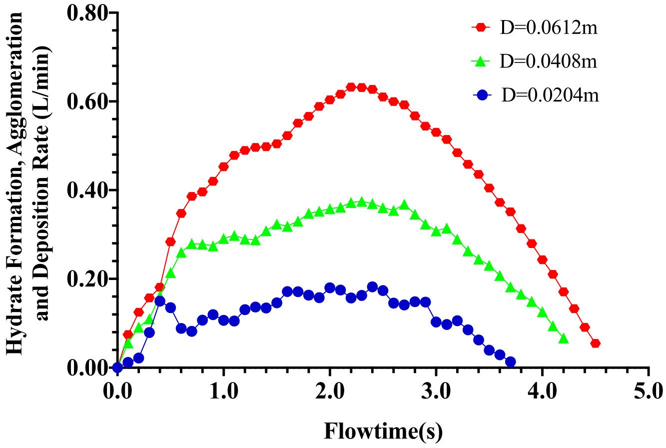

Fig. 34. Impact of change in pipe diameter on hydrate deposition rate at 8.8 m/s and 7.1 K subcooling temperature.

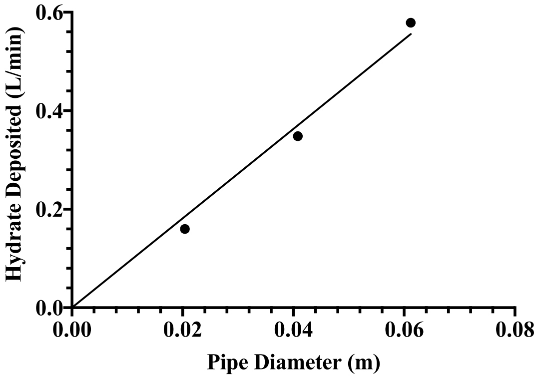

Fig. 35. Relationship between hydrate deposition rate and pipe diameter.

$$\frac{D_1}{D_2} = \frac{Q_{h\_d1}}{Q_{h\_d2}} \tag{25}$$

This can be modified with an extrapolation factor (K_{ex_factor}) as:

$$Q_{h\_d2} = K_{ex\_factor} \cdot \frac{D_2}{D_1} . Q_{h\_d1} \tag{26}$$

where Q_{h_d1} is the hydrate deposition rate predicted by this CFD model, L/min; Q_{h_d2} is the hydrate deposition rate estimated for actual design pipe, L/min; D_1 is the pipe diameter of this CFD model, 0.0204 m; D_2 is the pipe diameter of the actual pipeline, m; and K_{ex_factor} is the extrapolation factor (dimensionless), given a value of 1.1.

Eq. (26) indicates that increasing the diameter by a factor also increases the deposition rate by 1.1 times the same factor. For field application, the value of K_{ex_factor} can be modified based on field experience to estimate actual deposition rates of hydrates. Hence, by first entering the gas and water properties into this CFD model of diameter 0.0204 m and 10 m length, the hydrates deposition rate can be obtained, and is extrapolated for the purpose of design for the pipeline using Eq. (26).

3.10. *The relationship between velocity and shear stress on hydrate deposit*

The fluctuating gas shear stress on the pipe wall because of hydrate formation and deposition is important in providing insight into the possibility of hydrates deposition resulting in pipeline vibration (Jujuly et al., 2017). For the transportation of natural gas, the shear stress is defined by the Darcy friction factor and accounted for in the momentum equation (Coelho and Pinho, 2007). In multiphase turbulent flow computations, the primary carrier (gas) phase stress is related to the turbulent (eddy) viscosity ($\mu_{t_c} = \rho_c C_\mu \frac{k_c^2}{\varepsilon_c}$) discussed in Eq. (7). Earlier, the turbulent shear stress on the pipewall by the continuous carrier (gas) phase is mathematically defined as: $\tau_c^t = \overline{\alpha}_c \rho_c \left(\frac{2}{3}k - 2\frac{\mu_{t_c}}{\rho_c}.\nabla.\tilde{u}_c\right)$, in Eq. (17). By modifying this equation with the turbulent viscosity term above, we can have Eq. (27).

$$\tau_c^t = \overline{\alpha}_c \rho_c \left(\frac{2}{3}k - 2C_\mu \frac{k_c^2}{\varepsilon_c}.\nabla.\tilde{u}_c\right) \tag{27}$$

From the above mathematical relation, the shear stress can be influenced by turbulent kinetics (k), the phase volume fraction and density. Hence, decrease in turbulent kinetics of the hydrates deposited on the wall results in higher resisting shear within the water-hydrate composite. In this study, dissipation term is neglected to enhance deposition of hydrates at the wall. Implying, the water-induced shear stress on the deposited hydrates is expected to be higher than that of the gas within the hydrates (Charlton et al., 2018b). However, the increase in density of the gas phase from 79 to 83 kg/m^3 during the formation of hydrates can increase the shear stress of the gas phase slightly as indicated in Fig. 37 and Fig. 38. As explained in the turbulent Reynolds number plots (Fig. 32), to ensure that the hydrates shear stress was equivalent to the wall shear stress, it was important to achieve a $y^+<5$ for the flow of hydrates at 4.7 m/s and 8.8 m/s, so that the viscous force of the deposited hydrates at the wall will produce a no-slip condition (Fig. 36). The maximum y^+ at 4.7 m/s (2.5) and at 8.8 m/s (4.0) indicates that the water-induced shear stress on the layer of hydrates is equivalent to the pipe wall shear stress (Tu et al., 2018). The y^+ is defined in the literature (Fluent Theory, 2017; Tu et al., 2018), as indicated below.

$$y^+ = \frac{\rho y \mathrm{u}_\mathrm{r}}{\mu} \tag{28}$$

where ρ, y and μ, retains their earlier definitions. u_r, is related to wall shear stress and hydrates density as defined in the literature (Fluent Theory, 2017; Tu et al., 2018).

$$\mathrm{u}_\mathrm{r} = \sqrt{\frac{\tau_w}{\rho}} \tag{29}$$

Hydrates-induced wall shear stress can be defined from Eq. (28) and Eq. (29) as:

$$\tau_w = \frac{1}{\rho}\left(\frac{y^+\mu}{y}\right)^2 \tag{30}$$

From Eq. (28) and Eq. (29), the high viscosity of hydrates is responsible for the $y^+ < 5$. In Eq. (30), the increase in the viscosity of hydrates has a power of 2 effect, leading to high wall shedding shear stress by the deposited hydrates.

The main assumptions in deducing the predictions of the shear stress in this study are as follows: (i) the estimated shear stress is based on hydrate deposition only, and not on the pipe wall roughness because the pipe internal wall surface is smooth; (ii) the gas-induced shear stress is the sloughing shear stress because it is the carrier phase; and (iii) the water-induced shear stress on the hydrates is the wall shedding shear stress by the hydrate deposits because the hydrate deposit is in direct contact with the pipe wall. Determining the shear stress during hydrate sloughing and wall shedding is still an active area of research, with no consensus among scholars in this field of research on the nature of the shear stress during hydrate sloughing and wall shedding by hydrates. We proposed two shear stress regimes – a gas-induced shear stress responsible for hydrate sloughing, $\sigma_{sloughing}$, and water-induced shear stress leading to wall shedding by hydrates $\sigma_{shedding}$, such that $\sigma_{shedding} > \sigma_{sloughing}$. We define an operating shear stress ratio, σ_{op_ratio}, as follows.

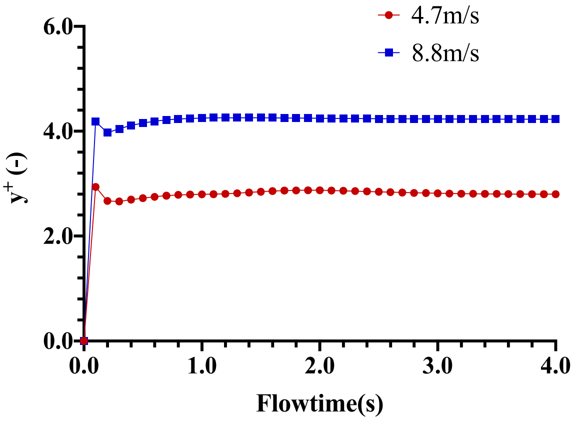

Fig. 36. Maximum y^+ plot at subcooling temperature of 7.0 K indicating that the simulation is dominated by viscous forces.

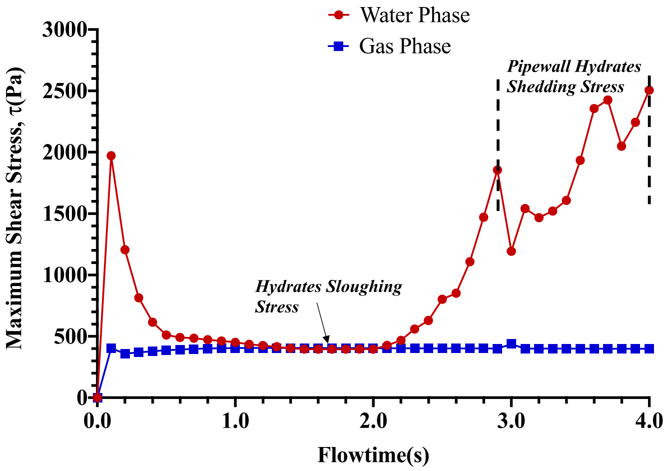

Fig. 37. Maximum shear stress on hydrate deposits at subcooling temperature of 7.0 K and at velocity of 8.8 m/s.

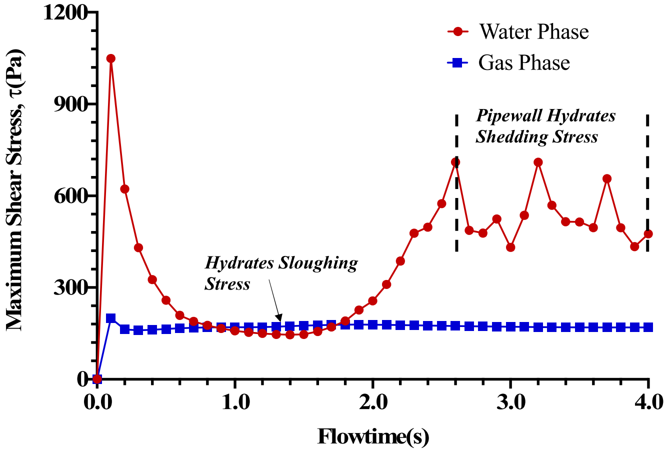

Fig. 38. Maximum shear stress on hydrate deposits at subcooling temperature of 7.0 K and at velocity of 4.7 m/s.

$$\sigma_{op\_ratio} = \frac{\sigma_{shedding}}{\sigma_{sloughing}} \tag{31}$$

This ratio is similar to the ratio of maximum to minimum shear stress proposed in (Aman et al., 2018). Liu et al. (2019) had argued in their paper that the position of Di Lorenzo et al. (2018) was inadequate in modelling hydrate rheology in the pipeline. However, the understanding posited in this paper clarifies why Di Lorenzo et al. (2018) assumed a constant shear stress in their analytical model on hydrate sloughing and Liu et al. (2019) assumed a fluctuating shear stress in their wall shedding analytical model. From our study, the constant shear stress is the gas shear stress for sloughing and the fluctuating shear stress is the water-induced shear stress for wall shedding by hydrates. Figs. 37 and 38 present the shear stress plots at gas velocities of 4.7 m/s and 8.8 m/s.

From Figs. 37 and 38, there is a steep rise in shear stress after 2.0 s, when the gas and water phase has formed hydrates. The shear stress induced from the water phase on the hydrate deposits from the flowtime of 2.5 s, increases at 8.8 m/s and fluctuates around 400 Pa at 4.7 m/s (Fig. 38). As the gas velocity increases from 4.7 m/s to 8.8 m/s, the gas shear stress also increased relatively by a factor of 1.5. This is as a result of increase in tangential velocity (Andreussi et al., 1985). The curves of the water-induced shear stress on the layer of hydrates in both velocity scenarios, agrees with the position of Liu et al. (2019) that the shear stress on hydrate deposit is not constant. Higher wall shedding of hydrates can be noticed at 8.8 m/s, while the wall shedding of hydrates at

4.7 m/s are relatively stable. Thus, assuming a uniform shear stress at lower velocity can be acceptable, but not at higher velocities. Although, sloughing has been studied in the literature with no concrete conclusion on the location of occurrence along the pipeline (Wang et al., 2018), the initial investigation by Aman et al. (2016) suggests that the ratio of the resisting water-hydrate composite shear stress to the flowing gas shear stress is 4.8. From Fig. 37 at 8.8 m/s, the average resisting shear stress is that of the water-hydrate composite (1934 Pa) and the flowing gas shear stress is 400 Pa, hence the ratio is 4.84. Similarly, at 4.7 m/s (Fig. 38) the ratio of the average resisting shear stress of the water-hydrate composite of 655 Pa to the corresponding flowing gas shear stress of 172 Pa is 3.81. The higher wall shear stress at 8.8 m/s implies a higher resistance to shear. Whereas there is a linearly growing hydrate layer at 8.8 m/s before wall shedding (Fig. 37), there is a uniformly stratified growing layer at 4.7 m/s before subsequent wall shedding (Fig. 38). However, this study suggests that higher minimum values of shear stress than the 100–200 Pa suggested in the literature (Aman et al., 2018; Di Lorenzo et al., 2018) is expected during sloughing at higher velocity, as the range stated in the literature only agree with our model prediction of 172 Pa at lower velocity of 4.7 m/s.

Similarly, from the indications in Figs. 37 and 38 we suggest the following. (1) at higher velocity of 8.8 m/s the operating shear stress ratio (Eq. (27)) is relatively equal to 1 ($\sigma_{op\_ratio} = 1$) during sloughing of hydrates, corresponding to the flowtime of 1.0–2.0 s when there was 2-phase gas and hydrates flow dominated by hydrate agglomeration. The rise in water-induced shear stress beyond 2.0 s until 2.8 s was to initiate the first wall shedding of hydrates as the hydrates agglomerates until the first deposition occurred at 2.8 s. Beyond this point, $\sigma_{op\_ratio} > 1$, encouraging wall shedding by hydrates. The shear stress fluctuates and increased in a linear order as more hydrate deposits from 2.8 s to the end of simulation flowtime. (2) at lower velocity of 4.7 m/s, $\sigma_{op\_ratio} = 1$ during hydrate sloughing, corresponding to the flowtime of 1.0–1.9 s when there was 2-phase gas and hydrate flow dominated by agglomeration of hydrates. The rise in water-induced shear stress beyond 1.9 s until 2.5 s was to initiate the first wall shedding of hydrates as the hydrates agglomerates until the first deposition occurred at 2.5 s. Beyond this point, $\sigma_{op\_ratio} > 1$, leading to wall shedding by hydrates. The shear stress fluctuates in a relatively stable manner as more hydrate deposits from 2.5 s to the end of simulation flowtime. Hence, we propose that the hydrate layer at the velocity of 8.8 m/s is a linearly growing annular profile, while the layer of hydrates at 4.7 m/s were deposited in a stratified annular pattern.

4. Conclusion-

The need for a specific gas-hydrates predicting model for gas-dominated systems has been stressed in the literature (Charlton et al., 2018a). Currently, both experimental and analytical research reports indicate the occurrence of hydrate deposition and gas shear stress on the pipe wall during hydrate sloughing and shedding along the pipe. However, this present work has developed a validated CFD model based on the fact that: (1) experiments are expensive and can hardly be extrapolated for actual field application; and (2) the need to improve on the predictions of the existing analytical model of Di Lorenzo et al. (2018). Based on the outcome of the analysis, the CFD model was able to accurately predict experimental and analytical results comparatively. The empirical results of this CFD model at 4.7 m/s and 8.8 m/s predicted both experimental and analytical model results within ±10% uncertainty bound. Consequently, the unique contributions of this work to knowledge include:

a. This novel CFD modelling approach improved hydrates deposition rate predictions at lower gas flow velocity of 4.7 m/s when compared with the only analytical model that predicted the deposition rates of hydrates at this velocity in gas-dominated pipeline.
b. As a proactive predictive tool, this CFD model can predict the deposition rates of hydrates using the system gas flow velocity, pressure, and temperature as inputs. Thus, serving as a real-time predictive tool for monitoring the plugging risk of hydrates in gas pipelines, unlike existing CFD modelling of the deposition of hydrates in the literature that requires external injection of hydrates into the flow domain.
c. The model also predicted the phase changes during the formation, agglomeration and deposition of hydrates, which is consistent with results from the analytical model of Wang et al. (2017) of 3-phase (gas, water and hydrates flow) and 2-phase (gas and hydrates flow).
d. The model simulation results using different pipe diameter led to a new proposition that the deposition rate of hydrates increases as the diameter of the pipe increases under the same boundary conditions. No prior study has reported this observation. This is useful in extending the CFD model for industrial application using a scaling factor.
e. In previous studies, Di Lorenzo et al. (2018) assumed a constant flowing shear stress, while Liu et al. (2019) assumed a varying shear stress value in their analytical models. This CFD model clarifies the disagreement as follows: (1) that the water-induced shear stress along the pipe fluctuates during wall shedding of hydrates as assumed in Liu et al. (2019); and (2) the gas-induced shear stress on the hydrates layer during hydrates sloughing is relatively constant as assumed in Di Lorenzo et al. (2018). By proposing a new ratio for the operating shear stress during sloughing and wall shedding, the model results compares favourably with the ratio of the resisting hydrates-water composite shear stress to the flowing gas shear stress on the deposit of hydrates suggested in Aman et al. (2016). The proposed 100–200 Pa shear stress during sloughing (Di Lorenzo et al., 2018) agrees with the predictions of this model at lower velocity of 4.7 m/s. However, this study suggests that higher values of shear stress than the value of 100–200 Pa suggested in the literature might be expected during sloughing at higher velocities.
f. We propose that the deposit of hydrates at the velocity of 8.8 m/s is a linearly growing annular profile, while the hydrates layer at 4.7 m/s were deposited in a stratified annular pattern.

While the CFD model can predict transient pressure drop during hydrates deposition and the resulting pipeline plugging flowtime, it is difficult to estimate both the actual transient pressure drop and plugging flowtime for an industry scale gas pipeline using the CFD model. Therefore, the need to combine the deposition rate of hydrates predicted in this model with an analytical model for estimating the actual plugging flowtime and resulting transient pressure drop for an industry size pipeline is identified as a gap for future studies. This identified gap is currently undertaken by the authors of this paper and will be the subject of future publication.

Credit author statement

Oghenethoja M. Umuteme: Conceptualization, Methodology, Software, Validation Data curation, Writing- Original draft preparation, Visualization, Investigation. Sheikh Zahidul Islam: Supervision, Conceptualization, Writing- Reviewing and Editing.; Mamdud Hossain: Supervision, Writing- Reviewing and Editing.; Aditya Karnik: Supervision, Writing- Reviewing and Editing.

Declaration of competing interest

The authors declare that they have no known competing financial interests or personal relationships that could have appeared to influence the work reported in this paper.

Data availability

Data will be made available on request.

Acknowledgement

The authors are grateful to the School of Engineering, Robert Gordon University, Aberdeen, United Kingdom, for supporting this research.

References

Abbasi, A., Hashim, F.M., 2014. Thermodynamic effects on hydrate formation in deepwater pipeline. In: Applied Mechanics and Materials. https://doi.org/10.4028/www.scientific.net/AMM.548-549.607, 607–611.

Aman, Z.M., Di Lorenzo, M., Kozielski, K., Koh, C.A., Warrier, P., Johns, M.L., May, E.F., 2016. Hydrate formation and deposition in a gas-dominant flowloop: initial studies of the effect of velocity and subcooling. J. Nat. Gas Sci. Eng. 1–9. https://doi.org/10.1016/j.jngse.2016.05.015.

Aman, Z.M., Qin, H., Pickarts, M., Lorenzo, M. Di, May, E.F., Koh, C.A., Zerpa, L.E., 2018. Deposition and shear stress initial investigations for hydrate blockage. In: Proceedings of the Annual Offshore Technology Conference. https://doi.org/10.4043/28777-ms.

Andreussi, P., Asali, J.C., Hanratty, T.J., 1985. Initiation of roll waves in gas-liquid flows. AIChE J. 31 https://doi.org/10.1002/aic.690310114.

Ashrafizadeh, A., Alinia, B., Mayeli, P., 2015. A new co-located pressure-based discretization method for the numerical solution of incompressible Navier-Stokes equations. Numer. Heat Tran. Part B Fundam. 67, 563–589. https://doi.org/10.1080/10407790.2014.992094.

BP, 2020. Statistical Review of World Energy 2020 (BP p.i.c, London).

Balakin, B.V., Lo, S., Kosinski, P., Hoffmann, C., 2016. Modelling agglomeration and deposition of gas hydrates technique. Chem. Eng. Sci. https://doi.org/10.1016/j.ces.2016.07.010.

Barron, R.M., Neyshabouri, A.A.S., 2003. Effects of under-relaxation factors on turbulent flow simulations. Int. J. Numer. Methods Fluid. 42, 923–928. https://doi.org/10.1002/fld.563.

Bbosa, B., Ozbayoglu, E., Volk, M., 2019. Experimental investigation of hydrate formation, plugging and flow properties using a high-pressure viscometer with helical impeller. J. Pet. Explor. Prod. Technol. 9, 1089–1104. https://doi.org/10.1007/s13202-018-0524-6.

Bendlksen, K.H., Maines, D., Moe, R., Nuland, S., 2004. The dynamic two-fluid model OLGA: theory and application. SPE Repr. Ser. 52–61.

Berrouk, A.S., Jiang, P., Safiyullah, F., Basha, M., 2020. CFD modelling of hydrate slurry flow in a pipeline based on Euler-Euler approach. Prog. Comput. Fluid Dynam. Int. J. 20, 156–168. https://doi.org/10.1504/PCFD.2020.107246.

Carroll, J., 2014. Natural Gas Hydrates: A Guide for Engineers, third ed. Gulf Professional Publishing, Waltham, MA 02451.

Charlton, T.B., Di Lorenzo, M., Zerpa, L.E., Koh, C.A., Johns, M.L., May, E.F., Aman, Z.M., 2018a. Simulating hydrate growth and transport behavior in gas-dominant flow. Energy Fuel. 32, 1012–1023. https://doi.org/10.1021/acs.energyfuels.7b02199.

Charlton, T.B., Zerpa, L.E., Koh, C.A., May, E.F., Aman, Z.M., 2018b. Predicting hydrate blockage formation in gas-dominant systems. In: Offshore Technology Conference Asia 2018, OTCA 2018. Offshore Technology Conference. https://doi.org/10.4043/28311-ms.

Chaudhari, P., Zerpa, L.E., Sum, A.K., 2018. A correlation to quantify hydrate plugging risk in oil and gas production pipelines based on hydrate transportability parameters. J. Nat. Gas Sci. Eng. https://doi.org/10.1016/j.jngse.2018.08.008.

Coelho, P.M., Pinho, C., 2007. Considerations about equations for steady state flow in natural gas pipelines. J. Brazilian Soc. Mech. Sci. Eng. 29, 262–273. https://doi.org/10.1590/S1678-58782007000300005.

Demirdzic, I., Gosman, A.D., Issa, R.I., Peric, M., 1987. A calculation procedure for turbulent flow in complex geometries. Comput. Fluids 15, 251–273. https://doi.org/10.1016/0045-7930(87)90009-0.

Di Lorenzo, M., Aman, Z.M., Kozielski, K., Norris, B.W.E., Johns, M.L., May, E.F., 2014a. Underinhibited hydrate formation and transport investigated using a single-pass gas-dominant flowloop. Energy Fuel. 28, 7274–7284. https://doi.org/10.1021/ef501609m.

Di Lorenzo, M., Aman, Z.M., Sanchez Soto, G., Johns, M., Kozielski, K.A., May, E.F., 2014b. Hydrate formation in gas-dominant systems using a single-pass flowloop. Energy Fuel. 28, 3043–3052. https://doi.org/10.1021/ef500361r.

Di Lorenzo, M., Aman, Z.M., Kozielski, K., Norris, B.W.E., Johns, M.L., May, E.F., 2018. Modelling hydrate deposition and sloughing in gas-dominant pipelines. J. Chem. Thermodyn. 117, 81–90. https://doi.org/10.1016/j.jct.2017.08.038.

Ding, L., Shi, B., Lv, X., Liu, Y., Wu, H., Wang, W., Gong, J., 2017. hydrate formation and plugging mechanisms in different gas-liquid flow patterns. Ind. Eng. Chem. Res. 56, 4173–4184. https://doi.org/10.1021/acs.iecr.6b02717.

Ferreira, G.G.S.S., Lage, P.L.C.C., Silva, L.F.L.R.R., Jasak, H., 2019. Implementation of an implicit pressure-velocity coupling for the Eulerian multi-fluid model. Comput. Fluids 181, 188–207. https://doi.org/10.1016/j.compfluid.2019.01.018.

Fox, R.O., 2014. On multiphase turbulence models for collisional fluid-particle flows. J. Fluid Mech. 742, 368–424. https://doi.org/10.1017/jfm.2014.21.

Jassim, E., Abdi, M.A., Muzychka, Y., 2010. A new approach to investigate hydrate deposition in gas-dominated flowlines. J. Nat. Gas Sci. Eng. 2, 163–177. https://doi.org/10.1016/j.jngse.2010.05.005.

Jujuly, M.M., Rahman, M.A., Maynard, A., Addy, M., 2017. Hydrate induced vibration in an offshore pipeline. In: Proceedings - SPE Annual Technical Conference and Exhibition. https://doi.org/10.2118/187378-ms.

Kader, B.A., 1981. Temperature and concentration profiles in fully turbulent boundary layers. Int. J. Heat Mass Tran. 24, 1541–1544. https://doi.org/10.1016/0017-9310(81)90220-9.

Kinnari, K., Hundseid, J., Li, X., Askvik, K.M., 2015. Hydrate management in practice. J. Chem. Eng. Data 60, 437–446. https://doi.org/10.1021/je500783u.

Koh, C., Creek, J., 2011. Safety in hydrate plug removal. In: Sloan, D., Koh, C.A., Sum, A. K. (Eds.), Natural Gas Hydrates in Flow Assurance. Gulf Professional Publishing: an imprint of Elsevier. https://doi.org/10.1016/B978-1-85617-945-4.00003-0, 37–48.

Lederhos, J.P., Long, J.P., Sum, A., Christiansen, R.L., Sloan, E.D., 1996. Effective kinetic inhibitors for natural gas hydrates. Chem. Eng. Sci. 51, 1221–1229. https://doi.org/10.1016/0009-2509(95)00370-3.

Lekvam, K., Bishnoi, P.R., 1997. Dissolution of methane in water at low temperatures and intermediate pressures. Fluid Phase Equil. 131, 297–309. https://doi.org/10.1016/s0378-3812(96)03229-3.

Li, W., Gong, J., Lü, X., Zhao, J., Feng, Y., Yu, D., 2013. A study of hydrate plug formation in a subsea natural gas pipeline using a novel high-pressure flow loop. Petrol. Sci. 10, 97–105. https://doi.org/10.1007/s12182-013-0255-8.

Li, P., Zhang, X., Lu, X., 2019. Three-dimensional Eulerian modeling of gas-liquid-solid flow with gas hydrate dissociation in a vertical pipe. Chem. Eng. Sci. 196, 145–165. https://doi.org/10.1016/j.ces.2018.10.053.

Li, Y., Liu, L., Jin, Y., Wu, N., 2021. Characterization and development of natural gas hydrate in marine clayey-silt reservoirs: a review and discussion. Adv. Geo-Energy Res. 5, 75–86. https://doi.org/10.46690/ager.2021.01.08.

Lim, V.W.S.S., Metaxas, P.J., Stanwix, P.L., Johns, M.L., Haandrikman, G., Crosby, D., Aman, Z.M., May, E.F., 2020. Gas hydrate formation probability and growth rate as a function of kinetic hydrate inhibitor (KHI) concentration. Chem. Eng. J. 388 https://doi.org/10.1016/j.cej.2020.124177.

Liu, W., Hu, J., Wu, K., Sun, F., Sun, Z., Chu, H., Li, X., 2019. A new hydrate deposition prediction model considering hydrate shedding and decomposition in horizontal gas-dominated pipelines. Petrol. Sci. Technol. 37, 1370–1386. https://doi.org/10.1080/10916466.2019.1587457.

Liu, Z., Vasheghani Farahani, M., Yang, M., Li, X., Zhao, J., Song, Y., Yang, J., 2020. Hydrate slurry flow characteristics influenced by formation, agglomeration and deposition in a fully visual flow loop. Fuel 277, 118066. https://doi.org/10.1016/j.fuel.2020.118066.

Lo, S., 2011. CFD modelling of hydrate formation in oil-dominated flows. Houston, Texas, USA. In: Offshore Technology Conference, OTC Offshore Technology Conference. https://doi.org/10.4043/21509-MS.

Lv, X., Yu, D., Li, W., Shi, B., Gong, J., 2012. Experimental study on blockage of gas hydrate slurry in a flow loop. Proc. Bienn. Int. Pipeline Conf. IPC 4, 37–43. https://doi.org/10.1115/IPC2012-90356.

Meindinyo, R.E.T., Svartaas, T.M., Nordbø, T.N., Bøe, R., 2015. Gas hydrate growth estimation based on heat transfer. Energy Fuel. 29, 587–594. https://doi.org/10.1021/ef502366u.

Melaina, M., Antonia, O., Penev, M., 2013. Blending hydrogen into natural gas pipeline networks: a review of key issues. Contract 303, 275–3000. https://doi.org/10.2172/1068610.

Meng, B., Gu, C., Zhang, L., Zhou, C., Li, X., Zhao, Y., Zheng, J., Chen, X., Han, Y., 2017. Hydrogen effects on X80 pipeline steel in high-pressure natural gas/hydrogen mixtures. Int. J. Hydrogen Energy 42, 7404–7412. https://doi.org/10.1016/j.ijhydene.2016.05.145.

Min, C.H., Tao, W.Q., 2007. An under-relaxation factor control method for accelerating the iteration convergence of flow field simulation. Eng. Comput. 24, 793–813. https://doi.org/10.1108/02644400710833314.

Mishriky, F., Walsh, P., 2017. Towards understanding the influence of gradient reconstruction methods on unstructured flowsimulations. Trans. Can. Soc. Mech. Eng. 41, 169–179. https://doi.org/10.1139/tcsme-2017-1012.

Mottaghian, P., Yuan, J., Piomelli, U., 2018. Boundary layer separation under strong adverse pressure gradient over smooth and rough walls. ERCOFTAC Ser 24, 173–179. https://doi.org/10.1007/978-3-319-63212-4_21.

Munson, B.R., Young, D.F., Okiishi, T.H., 1994. Fundamentals of fluid mechanics. Fundam. fluid Mech. https://doi.org/10.1201/b15874-3.

Munson, B.R., Okiishi, T.H., Huebsch, W.W., Rothmayer, A.P., 2013. Fundamentals of Fluid Mechanics, seventh ed. John Wiley & Sons, Inc., Hoboken, NJ.

Neto, E.T., Rahman, M.A., Imtiaz, S., Pereira, T., dos, S., Sousa, F.S. de, 2015. Coupled heat and mass transfer CFD model for methane hydrate 2-7. https://doi.org/10.1115/omae2015-42258.

Neto, E.T., Rahman, M.A., Imtiaz, S., Ahmed, S., 2016. Numerical flow analysis of hydrate formation in offshore pipelines using computational fluid dynamics (CFD). In: Proceedings of the International Conference on Offshore Mechanics and Arctic Engineering - OMAE. ASME, Busan, South Korea. https://doi.org/10.1115/OMAE2016-54534.

Odutola, T.O., Ajienka, J.A., Onyekonwu, M.O., Ikiensikimama, S.S., 2017. Fabrication and validation of a laboratory flow loop for hydrate studies. Am. J. Chem. Eng. Spec. Issue Oil F. Chem. Petrochemicals 5, 28–41. https://doi.org/10.11648/j.ajche.s.2017050301.14.

Peng, D.Y., Robinson, D.B., 1976. A new two-constant equation of state. Ind. Eng. Chem. Fundam. 15, 59–64. https://doi.org/10.1021/i160057a011.

Shih, T.-H., Liou, W.W., Shabbir, A., Yang, Z., Zhu, J., 1995. A new k-ε eddy viscosity model for high Reynolds number turbulent flows. Comput. Fluids 24, 227–238. https://doi.org/10.1016/0045-7930(94)00032-t.

Shyy, W., Thakur, S., Wrightt, J., 1992. Second-order upwind and central difference schemes for recirculating flow computation. AIAA J. 30, 923–932. https://doi.org/10.2514/3.11010.

Simonin, O., Viollet, P.L., 1990. Predictions of an oxygen droplet pulverization in a compressible subsonic coflowing hydrogen flow. Numer. Methods Multiph. Flows FED91 FED91, 65–82.

Skovborg, P., Rasmussen, P., 1994. A mass transport limited model for the growth of methane and ethane gas hydrates. Chem. Eng. Sci. 49, 923–932. https://doi.org/10.1016/0009-2509(94)85085-2.

Sloan, D.E., Koh, C.A., 2007. Clathrate hydrates of natural gases. In: Clathrate Hydrates of Natural Gases, third ed. CRC Press, Boca Raton, FL.

Sloan, E.D., Koh, C.A., Sum, A.K., 2011a. Six industrial hydrate blockage examples and lessons learned. In: Natural Gas Hydrates in Flow Assurance. https://doi.org/10.1016/b978-1-85617-945-4.00014-5, 171–191.

Sloan, E.D., Koh, C.A., Sum, A.K., 2011b. Natural Gas Hydrates in Flow Assurance. Gulf Professional Publishing: an imprint of Elsevier.

Song, G., Li, Y., Wang, W., Jiang, K., Shi, Z., Yao, S., 2018a. Numerical simulation of hydrate slurry flow behavior in oil-water systems based on hydrate agglomeration modelling. J. Pet. Sci. Eng. 169, 393–404. https://doi.org/10.1016/j.petrol.2018.05.073.

Song, G., Li, Y., Wang, W., Jiang, K., Shi, Z., Yao, S., 2018b. Numerical simulation of pipeline hydrate particle agglomeration based on population balance theory. J. Nat. Gas Sci. Eng. 51, 251–261. https://doi.org/10.1016/j.jngse.2018.01.009.

Sule, I.O., Adedeji, A., Obeng, C., Okosun, A., Morshed, M., Rahman, M.A., Hawboldt, K., 2015. CFD analysis of hydrate formation in pipelines. Petrol. Sci. Technol. 33, 571–578. https://doi.org/10.1080/10916466.2014.994708.

Fluent Theory, 2017. ANSYS Fluent Theory Guide Version 18.1. ANSYS, Inc., 275 Technology Drive Canonsburg,, 275 Technology Drive Canonsburg, PA 15317.

Tu, J., Yeoh, G.H., Liu, C., 2018. Computational fluid dynamics: a practical approach. In: Computational Fluid Dynamics, third ed. Butterworth-Heinemann. https://doi.org/10.1016/b978-0-08-101127-0.09979-7.

Turner, D., Talley, L., 2008. Hydrate inhibition via cold flow - No chemicals or insulation. In: Proceedings of the 6th International Conference on Gas Hydrates (ICGH 2008). Vancouver, British Columbia, Canada. https://doi.org/10.14288/1.0041089. July 6-10, 2008.

Turner, D., Boxall, J., Yang, D., Kleehamer, C., Koh, C., Miller, K., Sloan, E.D., Yang, S., Xu, Z., Mathews, P., Talley, L., 2005. Development of a hydrate kinetic model and its incorporation into the OLGA2000® transient multi-phase flow simulator. In: Proc. 5th Int. Conf. Gas Hydrates.

Umuteme, O.M., 2020. Computational fluid dynamics (CFD) transient pressure and temperature simulation of a natural gas - hydrogen gas transportation pipeline. Int. J. Innov. Res. Dev. 9, 112–116. https://doi.org/10.24940/ijird/2020/v9/i6/JUN20056.

Umuteme, O., Umeh, E., 2019. A mechanistic approach to subsea gas pipeline capacity utilization - case study. In: Society of Petroleum Engineers - SPE Nigeria Annual International Conference and Exhibition 2019. https://doi.org/10.2118/198767-MS. NAIC 2019.

Vakilipour, S., Mohammadi, M., Badrkhani, V., Ormiston, S., 2019. Developing a physical influence upwind scheme for pressure-based cell-centered finite volume methods. Int. J. Numer. Methods Fluid. 89, 43–70. https://doi.org/10.1002/fld.4682.

Vysniauskas, A., Bishnoi, P.R., 1983. A kinetic study of methane hydrate formation. Chem. Eng. Sci. 38 https://doi.org/10.1016/0009-2509(83)80027-X.

Wang, Z., Zhang, J., Sun, B., Chen, L., Zhao, Y., Fu, W., 2017. A new hydrate deposition prediction model for gas-dominated systems with free water. Chem. Eng. Sci. 163, 145–154. https://doi.org/10.1016/j.ces.2017.01.030.

Wang, Z., Zhang, J., Chen, L., Zhao, Y., Fu, W., Yu, J., Sun, B., 2018. Modeling of hydrate layer growth in horizontal gas-dominated pipelines with free water. J. Nat. Gas Sci. Eng. 50, 364–373. https://doi.org/10.1016/j.jngse.2017.11.023.

Yin, Z., Khurana, Maninder, Tan, Hoon Kiang, Linga, Praveen, Khurana, M., Tan, H.K., Linga, P., 2018. A review of gas hydrate growth kinetic models. Chem. Eng. J. 342, 9–29.

Yongchao, R., Yi, S., Shuli, W., Ru, J., 2019. Numerical simulation study on the law of attenuation of hydrate particles in a gas transmission pipeline. Energies 12. https://doi.org/10.3390/en12010058.

Zerpa, L.E., Rao, I., Aman, Z.M., Danielson, T.J., Koh, C.A., Sloan, E.D., Sum, A.K., 2013. Multiphase flow modeling of gas hydrates with a simple hydrodynamic slug flow model. Chem. Eng. Sci. 99, 298–304. https://doi.org/10.1016/j.ces.2013.06.016.

Zhang, P., Wu, Q., Mu, C., 2017. Influence of temperature on methane hydrate formation. Sci. Rep. 7 https://doi.org/10.1038/s41598-017-08430-y.